Understanding novel gap-bridged remote laser welded (RLW) joints for automotive high-rate and temperature applications

Abhishek Das, Iain Masters, David Williams

WMG, The University of Warwick, Coventry, CV4 8GJ, United Kingdom

E-mail: A.Das.1@warwick.ac.uk

Abstract:

This paper investigates the microstructure, high-rate and temperature dependent tensile behaviour of fillet edge joints produced by novel 'gap-bridged' remote laser welding (RLW) using an automotive grade aluminium alloy AA6014, commercially known as AC-170PX, extensively used for automotive skin panel applications. Three part-to-part gap-bridged RLW fillet edge welds, produced with different gaps (0.2 mm, 0.4 mm and 0.6 mm) were examined for joint geometry and microstructure. Relatively larger columnar grains resulting from directional solidification were observed in the fusion zone and microhardness was reduced by ~15- 20% due to precipitates disappearance. Moderate (0.1 m/s) to high speed rate (10 m/s) tensile tests performed at room temperature (~23°C) were used to determine high-rate tensile performance. Although the strain rate dependency was found to be low, an increase in tensile extension was obtained. Additionally, the joint tensile performance was evaluated over a range of temperatures between -50°C and 300°C. Using digital image correlation (DIC), fracture strains were obtained in the range from 0.21 to 0.25 for all gap and speed conditions. Fusion zone based finite element simulations were performed using the Johnson-Cook material failure model to predict joint strength. Additionally, the suitability of gap-bridged RLW joints for automotive applications was determined by comparison with two industrial joining methods, self-piercing riveting (SPR) and resistance spot welding (RSW).

Keywords: Remote laser welding; Weld microstructure; High-rate tensile performance; Strain distribution; Temperature response; Finite element modelling

1. Introduction

Due to several advantages including high-strength-to-weight ratio, formability and higher crash-energy absorption, aluminium alloys are widely used in various transport industries [1]. For example, aluminium alloys are increasingly being used in the automotive and rail sectors for developing structural parts, body-in-white assemblies or skin panels [2, 3]. Additionally, automotive vehicles are required to meet the ever more stringent emission targets set out by the different national and international legislative authorities [4, 5]. As a result, a number of corrective and preventive actions are undertaken by automotive manufacturers including the development of electric vehicles [6, 7]; alternative source of energy harnessing, e.g. fuel cell [6]; or improvement of existing internal combustion engines [8]. One approach common to several automotive manufacturers is the adoption of aluminium alloys to reduce the vehicle body weight. AA6xxx series aluminium alloys (AlMgSi) are widely used for automotive outer skin panel applications [9] and also for battery casing/ housing on electric vehicles (EVs) [10, 11] due to their good mechanical properties, formability, enhanced corrosion resistance and hemming capabilities. Commercially available AC-170PX (AA6014) is predominantly used for making closure/hang-on panels but is also suitable for demanding inner structural or battery casing applications [12]. Although the use of aluminium alloys can help to reduce the weight of the structures, welding of aluminium alloys is not trivial due to the presence of an aluminium oxide layer, high thermal conductivity and high thermal expansion coefficient [13, 14]. Making satisfactory welded joints poses a real challenge for aluminium alloys since porosity formation and hot cracking are common phenomena observed during welding.

The sheet metal parts used in automotive body-in-white applications are generally produced using stamping. Due to the inherent variability of the stamping operation and intrinsic flexibility of sheet metal, the produced parts contain dimensional and geometrical errors

compared to the nominal design (i.e. CAD design) [15, 16]. These dimensional and geometric errors result in part-to-part gaps at assembly. Mitigating these part-to-part gaps during the welding operation is a critical challenge to ensure the performance of the final assembly. A number of methods have been adopted by researchers to minimise/eliminate the part-to-part gaps at assembly including tighter tolerances [17, 18], fixture optimisation [19] and adapting suitable joining processes. Despite such measures, part-to-part gaps up to 0.6 mm are common during assembly [20, 21]. Due to more demanding assembly requirements, a novel 'gap-bridging' process using the remote laser welding (RLW) technique is emerging as an alternative solution to bridge the part-to-part gaps during welding [22]. By combining the benefits from RLW (e.g. high throughput, floor space reduction and cost) with the gap-bridging technique, aluminium sheet metal assemblies can be successfully produced, and current aluminium joining techniques such as resistance spot welding or self-piercing riveting can be replaced. Joint quality is often assessed on strength performance but evaluation of weld microstructure is equally important. However, the quasi-static tensile evaluation may not be sufficient for automotive applications where an understanding of joint performance during crash events is essential [1]. Therefore, it is necessary to characterise the high-rate tensile performance along with the microstructural evaluation of the joint. To address these identified gaps, this study explores the feasibility of using remote laser welding to bridge three levels of the part-to-part gap in a fillet edge joint using AC-170PX aluminium alloy. The joint strength is then characterised at high strain rates.

1.1. *Review of weld microstructure and high-rate characterisation*

In general, the RLW gap-bridging technique is applied to produce fillet edge welds. The principle of RLW gap-bridging is explained by Fixemer, et al. [21] where an oscillated laser beam has been proven to achieve part-to-part gap bridging [14]. Being a newly developed technique, limited information is available in the literature on fillet edge weld microstructure

characterisation and subsequent high-rate tensile characterisation. Alshaer, et al. [23] reported an investigation to identify the effect of laser parameters on weld microstructure when AC-170PX (AA6014) aluminium alloy was laser welded with an AlSi5 (AA4043) filler wire using *near-field or conventional laser* welding. In contrast, RLW is an autogenous process where no filler wire or shield gas is used. Only a few investigations have been conducted on 6xxx series aluminium alloys to understand the occurrence of hot cracks in overlap joint conditions [24, 25]. Albert, et al. [22] reported the weldability of steel and aluminium alloys to produce fillet edge weld under different part-to-part gap conditions. Using AA5182 aluminium alloys, Das, et al. [14] reported the effects of laser power and welding speed on microstructure and subsequent evaluation of tensile strength using the lap shear test. The tensile characterisation was conducted at a slow rate of speed i.e. 2 mm/min. However, high-rate characterisation is also important to identify the behaviour of fillet edge weld during crash conditions. The detailed gap-bridging of AC-170PX (AA6014) aluminium alloy and subsequent high-rate characterisation are missing from the literature.

Generally, aluminium alloys are considered to have low strain rate sensitivity [26, 27] and most high-rate characterisation has been performed purely on the parent material. A few works have been reported using 6xxx series aluminium alloys and often a negative strain rate was observed [26, 28]. Chen, et al. [29] investigated AA6060 and AA6082 parent material and reported that they exhibited only slight sensitivity to the strain rate, and could probably be modelled as rate-insensitive with good accuracy. For automotive applications where crash behaviour is important, it is necessary to evaluate the joint performance under high-rate tensile testing.

1.2. *Review of depressed and elevated temperature performance*

Similar to high strain rate characterisation, limited studies are reported in the literature on depressed and elevated temperature characterisation. Most of these studies focused on parent material thermal softening rather than the joint characterisation. However, laser welded joints

used in battery casings for electric vehicles needed to be tested at elevated or depressed temperatures to emulate conditions in a battery thermal runaway or cryogenic transport [30, 31]. To understand the performance of aluminium alloys during a fire, Summers, et al. [32] reported high temperature quasi-static mechanical behaviour of 5083-H116 and 6061-T651 where a gradual decrease in ultimate strength was measured with the higher temperature between 200 – 350°C. Various aluminium alloys were tested at temperatures ranging from room temperature to 300 °C to understand the variability in the thermo-mechanical behaviour [33], the effect of temperature on dynamic tensile flow stress [34] or generic properties such as tensile strength, creep and fatigue [35]. It was found that flow stress decreased with increase in temperature and beyond 200 °C thermal softening was the predominant mode of deformation mechanism. Similarly, parent material uniaxial tensile tests were conducted on AA5182-O at temperature levels of 25, 100, 200 and 300 °C using slow to moderate strain rates [36] and flow stress was found to decrease with the increase of temperature. However, the aforesaid characterisation is basically focused on parent material testing at elevated temperatures. Therefore, there is a need to further characterise RLW fillet edge joints to establish their responses at depressed and elevated temperatures.

1.3. *Research gap and objectives*

Microstructural inspection and slow rate tensile performance are reported in the literature for aluminium alloy based laser joining applications [14, 37]. However, no gap based feasibility study has been reported using AC-170PX and corresponding tensile properties were measured at a slow rate [9]. The research work reported in the literature and identified research gap are summarised in Table 1.

Table 1 Research studies reported in the literature on microstructure and tensile characterisation of RLW fillet edge welds and identified research gap addressed in this paper.

Part-to-part gap	Microstructure and slow rate tensile characterisation	Microstructure, high-rate and temperature based tensile characterisation
Zero or no gap	Roos and Schmidt [38] Das, et al. [9] Das, et al. [14]	-
Higher than zero-gap	Albert, et al. [22] Müller, et al. [39] Das, et al. [14]	*To be addressed in this paper using AC-170PX aluminium alloy*

The RLW part-to-part gap-bridged fillet edge weld and its typical key geometrical characteristics (i.e. penetration, leg length and throat thickness) are shown in Figure 1. The aforesaid research gap is to be addressed in this paper by fulfilling the following objectives: (i) evaluation of the fusion zone geometries and microstructures using electron backscatter diffraction (EBSD) maps and microhardness distributions; (ii) determining the high speed tensile performance of the gap-bridged fillet edge joints; (iii) strain mapping across the joint using digital image correlation; (iv) understanding the tensile performance under depressed and elevated temperatures, (v) development of fusion zone based finite element models to simulate the joint performance at the room as well as depressed and elevated temperatures, and (vi) comparison of RLW gap-bridged joints with other industrial joining processes, such as resistance spot welding (RSW) and self-piercing riveting (SPR).

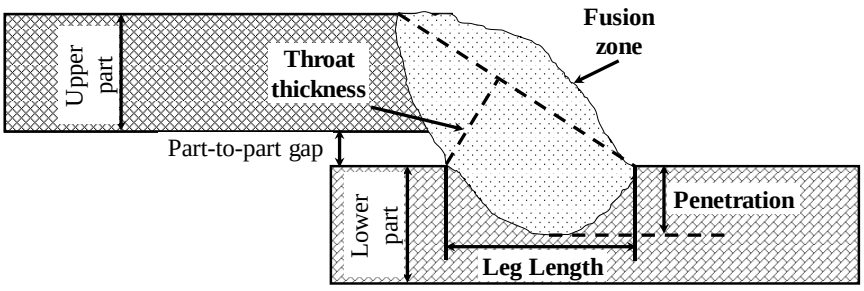

Figure 1 Key geometrical features of part-to-part gap-bridged RLW fillet edge weld [14, 40].

2. Materials and experimental procedure

2.1. Details of Substrate Materials

It has been reported that up to 37% of an automotive body is made of AA6xxx series aluminium alloys [41]. Heat treatable AC-170PX (i.e. AA6014) aluminium alloy is widely used for automotive body-in-white skin panels as well as structural applications where high formability and good surface quality are required [42]. The extremely good bendability (i.e. the basic requirements of sharp hemming operation) of AC-170PX, make it particularly useful for the production of closure panels [12] and for this reason AC-170PX has been chosen for this experimental investigation. The chemical composition of AC-170PX parent material is given in Table 2.

The stress-strain behaviour, as shown in Figure 2(b), was determined using a dog-bone specimen (Figure 2(a)) as per BS EN ISO 527- 1 [43] and an Instron 5800 test frame with a 100 kN load capacity and axial video extensometer. The physical and mechanical properties of the base material are listed in Figure 2(c). These base material properties are utilised for the high-rate tensile characterisation and subsequent FE modelling.

Table 2 Chemical composition (wt %) of AC-170PX (AA6014) aluminium alloy used in this study.

Alloy Grade	Si	Fe	Cu	Mn	Mg	Cr	Zn	Ti	V	Others	Al
AA6014	0.5-0.7	0.35	0.25	0.05-0.20	0.40-0.8	0.20	0.10	0.10	0.50-0.20	0.15	Remaining

(a)

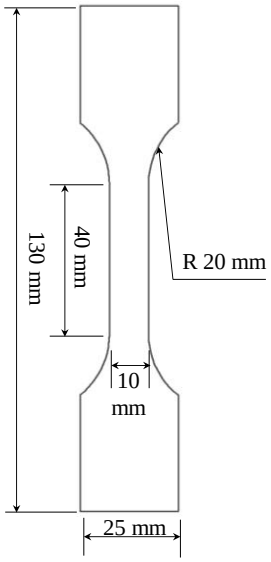

(b)

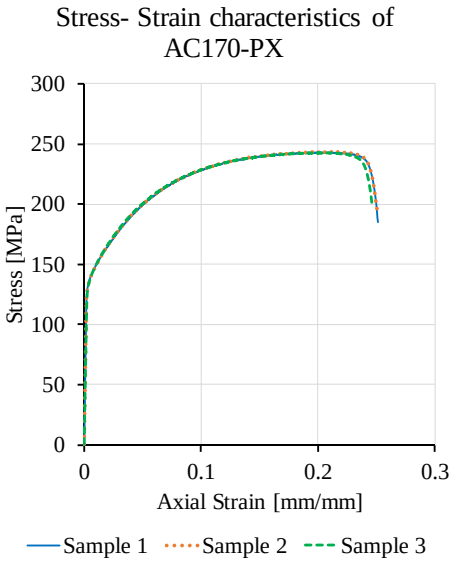

(c)

Properties	Unit	AA6014
Yield strength (0.2%)	MPa	120
Tensile Strength, UTS	MPa	244
Maximum tensile load	N	2732.7
Tensile extension at maximum load	mm	8.29
Density	kg/m^3	2.7×10^3
Young's modulus, E	GPa	68.9
Shear modulus	GPa	26
Poisson's ratio	-	0.33

Figure 2 (a) Schematic of the tensile specimen of AC170-PX base material, (b) Stress-strain behaviour of the base material (BM), (c) Physical and mechanical properties of AC-170PX (AA6014) aluminium alloy [42].

2.2. RLW assembly and experimental details

Optical seam tracking using an integrated remote laser welding-automatic (RLW-A) optical head by Scansonic was employed to produce the gap-bridged fillet edge welds. This system enables accurate tracking of the fillet edge and also detects the part-to-part gap in between the upper and lower parts. The laser source was a TRUMPF TruDisk 5001 having a maximum power of 5 kW and an IR wavelength of 1030 nm. The laser was delivered by a fibre of 200 µm in diameter and the nominal focal distance was 500 mm with a nominal spot size of 580 µm. Laser welding for sheet metal parts can be classified into near-field or conventional laser welding and far-field or remote laser welding (RLW) [14, 23]. Unlike conventional laser welding, RLW is an autogenous process which does not use filler wire or shielding gas.

For this gap-bridging experimental investigation, three part-to-part gaps (i.e. 0.2 mm, 0.4 mm and 0.6 mm) were created during welding of the parent assembly by placing packing shims in between the parent sheets which had dimensions of 450 mm × 175 mm. These identical AC-

170PX sheets of 1.1 mm thickness were assembled by overlapping the upper and lower sheets by 25 mm along the long edge as shown in Figure 3. RLW gap-bridging works on the principle of beam oscillation and/or beam defocusing to bridge the part-to-part gaps [39]. Optical seam tracking based laser triangulation is used to determine the gap height between the sheets and setting angles of the optics in reference to the workpiece [22]. Commonly investigated part-to-part gaps reported in the literature are mostly less than 0.6 mm [23, 44]. To further investigate the effects of typical gaps found in production, this study used 0.2 mm, 0.4 mm and 0.6 mm part-to-part gaps for microstructural characterisation of the fillet edge welds and to evaluate high-rate tensile performance. Pilot runs were conducted to obtain feasible ranges of laser process parameters to produce a 'good-weld' where (i) the penetration depth should be higher than 0.2× lower sheet thickness to obtain satisfactory lap shear strength, and (ii) the penetration depth should be lower than 0.7× lower sheet thickness to avoid full penetration and bottom surface convexity [14].

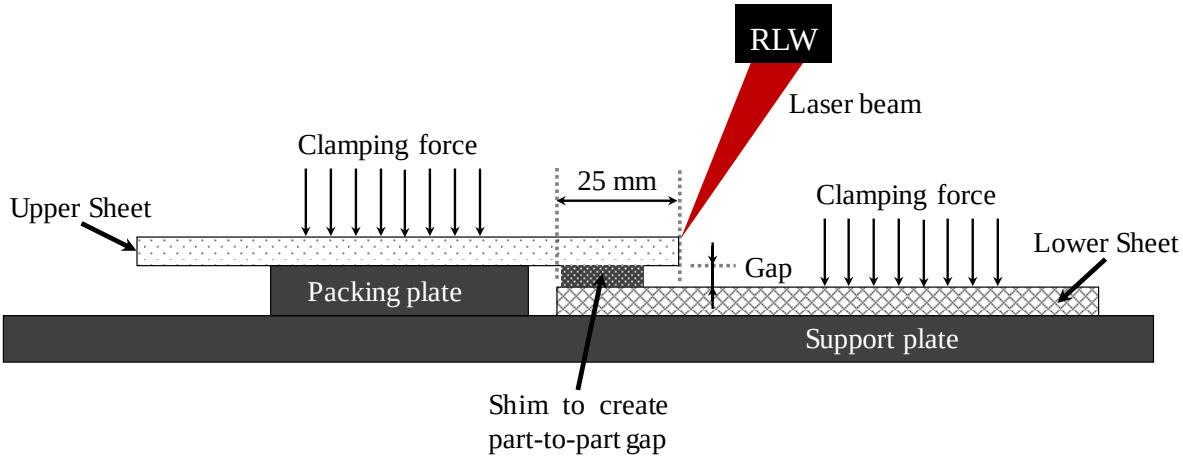

Figure 3 Schematic of the parent assembly configuration to create gap-bridged fillet edge weld using RLW.

Relying on these pilot tests and weld quality criteria, the remote laser welding parameters were chosen to produce 'good-welds' as listed in Table 3. As the RLW is an autogenous process where additional filler wire is not applied to fuse the gap between two parts, it is essential to

bridge the gap by melting additional material from the upper part to fuse with the lower part. To achieve this, the laser power was gradually increased with increasing part-to-part gap based on the results of pilot screening tests.

Table 3 RLW process parameters used to produce gap-bridged fillet edge welds.

Sl No	Part-to-part gap [mm]	Laser Power [kW]	Welding Speed [m/min]
1	0.2	3.3	4.0
2	0.4	3.6	4.0
3	0.6	3.9	4.0

2.3. Details of specimen preparation and high-speed test conditions

After carrying out the remote laser welding, samples were prepared for metallographic inspection and subsequent high-rate tensile characterisation. To investigate the fusion zone, metallographic samples were cut perpendicular to the welding direction and then mounted in a conductive thermosetting phenolic compression resin. Subsequently, the mounted samples were polished using p400 SiC grit paper, 9 µm and 3 µm diamond suspension solutions, and thereafter, 0.02–0.06 µm colloidal silica solution as a final stage of polishing. To obtain the microstructure of base material, heat affected zone and fusion zone, the polished samples were etched in Barker's reagent (5 ml Tetra-fluoroboric acid, HBF4 + 100 ml of water) for 120 seconds. Using a Nikon Eclipse LV150N optical microscope, the weld microstructures were examined, especially the penetration depth, leg length and throat thickness. Microhardness profiles were measured using 300 gf ($HV_{0.3}$) load and a test duration of 10s. A Carl Zeiss Sigma scanning electron microscopy (SEM) equipped with field emission gun, was used for energy dispersive spectroscopy (EDS) and electron backscatter diffraction (EBSD) analysis.

From the parent assembly, tensile samples 29 mm in width were prepared as adapted from BS EN ISO 26203-2 [45] and Wood, et al. [46]. Typically for automotive applications, materials

were tested over a range of high-rates as recommended in ESIS [47], Wood, et al. [46]. For high-rate tensile characterisation, an Instron precision servo-hydraulic VHS 160/100-20 machine was used which has the capability to perform tests in the range of 10 mm/s to 20 m/s and has been rated to a maximum impact force of 100 kN. A wide range of test speeds is reported in the literature, for example, Wood, et al. [48] performed tests on self-piercing riveted aluminium joints in the range of 1.0 mm/s to 5.0 m/s. Additionally, Liu, et al. [49] conducted high-rate dynamic tensile tests at 0.1, 1.0, 5.0 and 10.0 m/s on the base material and laser welded butt joint using DP780 steel. In typical automotive crash/accident studies, the experienced strain rates occur in the range between moderate (0.1 m/s) and high-rate (10 m/s) [48, 50]. Based on these reports and as recommended by Wood, et al. [46], the RLW gap-bridged fillet edge welds were tested at speeds from moderate (0.1 m/s) to high-rate (10 m/s). Three repetitions were performed at 0.1 m/s, 1.0 m/s, 5.0 m/s and 10.0 m/s on test specimens produced with different part-to-part gap values as listed in Table 3.

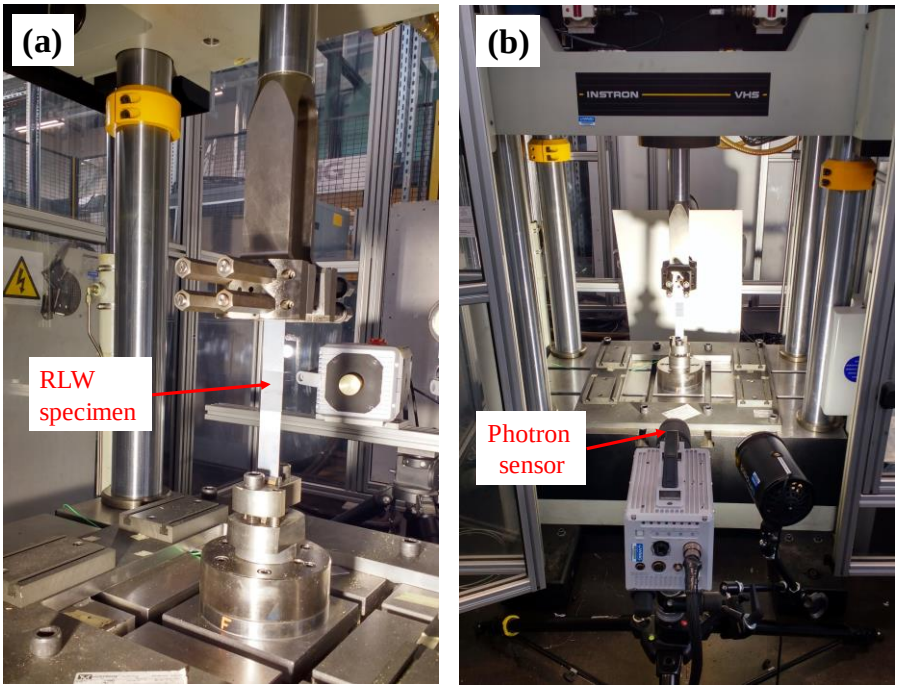

Figure 4 High-speed test set-up (a) RLW specimen mounted in Instron precision servo-hydraulic VHS 160/100-20, and (b) high-speed image capturing using a Photron sensor with external light to illuminate the investigated speckle pattern surface.

During the tests, the dynamic strain development was captured in a series of images using a non-contact high speed Photron FASTCAM SA-X2 monochrome camera. These images were subsequently used in a full-field strain measuring system i.e. GOM Aramis platform to evaluate strain development at various test speeds based on the digital image correlation (DIC) method [51]. To capture the strain occurring during the tests, the tensile samples were first painted matt black over which a random white speckle pattern was applied. The relative movement of these speckles from image to image was used to study the deformation process of the specimens up to fracture. The high-rate test set-up for RLW specimen in the Instron VHS test frame and the Photron camera are shown in Figure 4. In this study, 1000, 20000, 50000, and 80000 fps (i.e. frames per second) were used from the start of the tensile tests until fracture occurred for the test speeds of 0.1, 1.0, 5.0, and 10.0 m/s, respectively. Typically, an increase in frame rate has a detrimental effect on the resolution. Therefore, the same resolution cannot be used for both slow and high-speed tests. The image resolutions used to capture deformation behaviour were 1024 × 1024, 1024 × 1024, 384 × 560 and 384 × 336 for the test speeds of 0.1, 1.0, 5.0, and 10.0 m/s, respectively where pixel width/height of each image was 0.105 mm.

The depressed and elevated temperature tests were performed using the same Instron test frame fitted with a thermal chamber which operates between -50 °C and 350 °C. The temperature was controlled using the in-built thermocouple and an additional thermocouple attached to the static side of the test sample for accurate measurement of sample temperature. In addition to room temperature (~23°C) tests, the RLW joints were tested at -50°C, 0°C, 50°C, 100°C, 200°C, and 300°C to identify the effects of depressed and elevated temperatures. All the temperature tests were performed at 0.1 m/s in order to minimise the noise in the test data. As the thermal chamber needs to be placed below the upper grip, a total specimen length of 525 mm was required. This was achieved by overlapping 450 mm × 175 mm and 450 mm × 375 mm sheets by 25 mm along their welding edges. After the welding, these parent assemblies were cut into

29 mm with strips for temperature based joint strength characterisation. The depressed temperatures (i.e. -50°C and 0°C) were obtained using liquid nitrogen whereas the elevated temperatures were attained using the in-built heating coil within the thermal chamber.

3. Experimental results and discussions

3.1. Base material microstructural properties

The scanning electron microscopy (SEM) image of the AC170-PX base material (BM) in Figure 5(a) confirms that the precipitates or the second phase materials are evenly distributed within the BM. Energy dispersive spectroscopy (EDS) analysis of the precipitates shows that the darker phase contains Al-Mg-Si and the lighter phase consists of Al and Fe, as shown in Figure 5(c)-(d). The grain structure of the BM is shown in Figure 5(b), where the average grain size was 18 μm obtained using the linear intercept method.

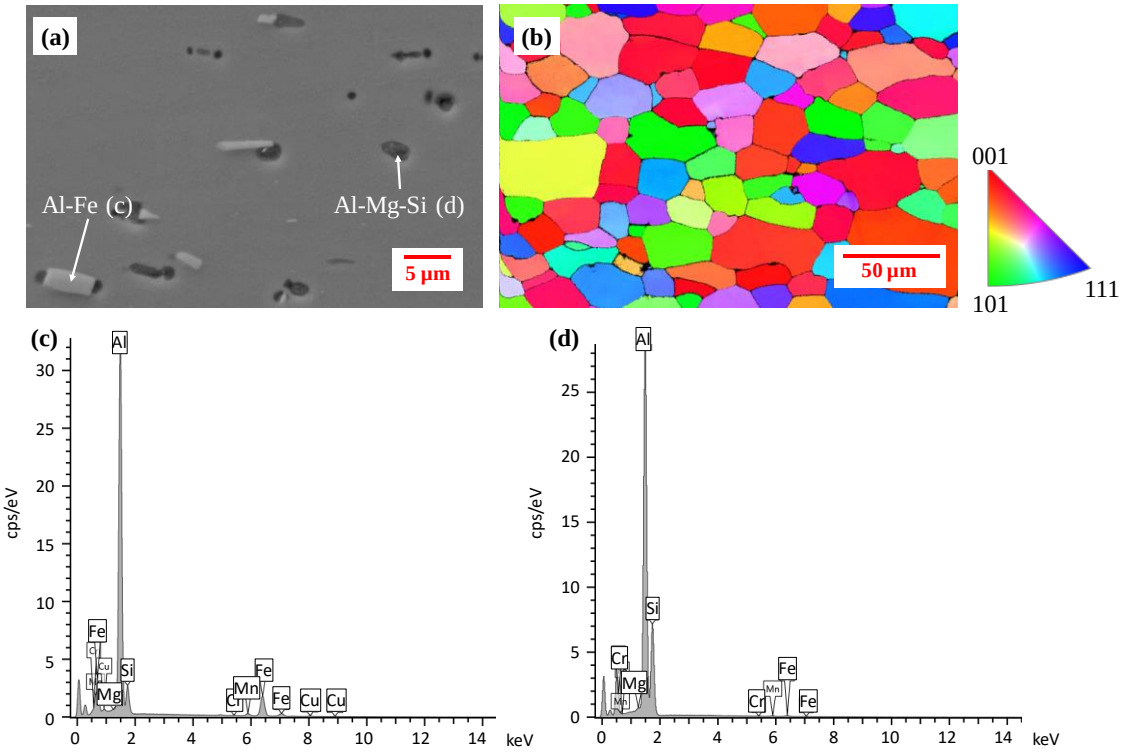

Figure 5 AC170-PX base material (a) SEM micrograph of phase distribution, (b) grain structure from electron backscatter diffraction (EBSD) image, (c) EDS analysis for Al-Fe precipitates, and, (d) EDS analysis for Al-Mg-Si precipitates.

3.2. Joint geometrical features and properties

The key geometrical features i.e. penetration depth, leg length and throat thickness as defined in Figure 1, were obtained at low magnification (×5) using a Nikon Eclipse LV150N optical microscope. Figure 6 (a) - (c) illustrate the cross-sectional micrographs obtained from 0.2 mm, 0.4 mm and 0.6 mm part-to-part gap-bridged fillet edge welds.

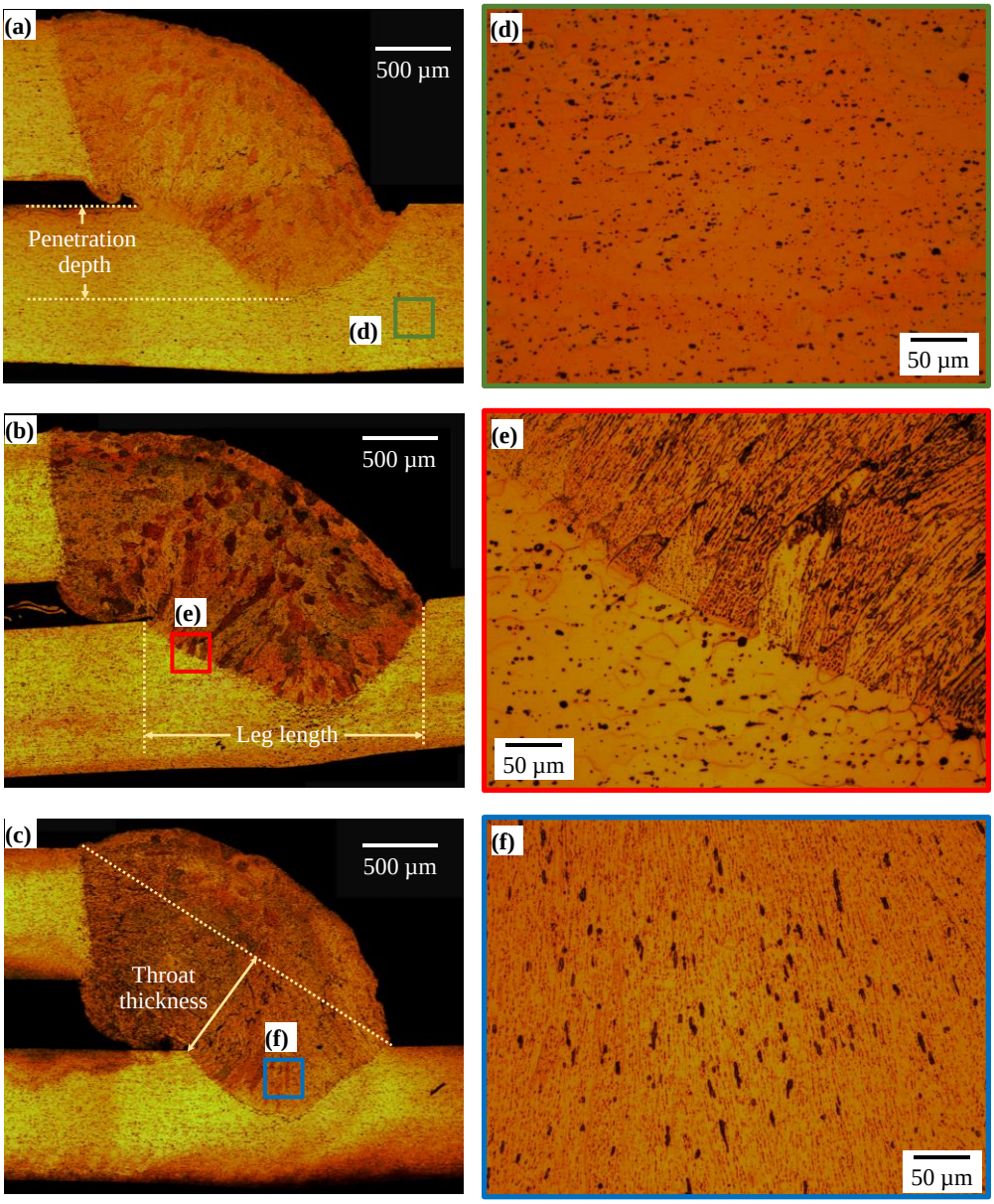

Figure 6 Cross-sectional images of RLW gap-bridged fillet edge welds for (a) 0.2 mm gap, (b) 0.4 mm gap, (c) 0.6 mm gap, (d) base material (BM), (e) transition from BM to FZ, and (f) fusion zone (FZ).

It is evident from these cross-sectional micrographs that they were composed of two distinctive regions, namely, the fusion zone (FZ) and base material (BM). Due to the application of laser energy, the upper and lower parts at the point of laser beam application were melted and resolidified to form the FZ. At the interface between the fusion zone and base material, there is an area of a base material which was not melted but had its microstructure and properties altered by the heat input, known as heat-affected zone (HAZ) [23]. Laser welding is a fast joining process compared to other conventional welding processes with higher localised heat input, produces a very narrow HAZ not visible at lower magnification. In general, columnar grain growth was observed from the fusion boundary (i.e. transition from BM to FZ) towards the centre of the fusion zone [52]. Figure 6(e) shows the transition from the base material to the fusion zone where the elongated grains are visible. Microstructural inspection revealed the values of penetration depth, leg length and throat thickness obtained from the three part-to-part gap bridged fillet edge welds.

For the RLW fillet edge weld, Das, et al. [14] defined the criteria for under-weld and over-weld, if the penetration depth was below 0.2 times and above 0.7 times the lower sheet thickness, respectively. A weld having a penetration depth in between these values is considered a good weld. The average penetration depths obtained from the 0.2 mm, 0.4 mm and 0.6 mm gap bridged fillet edge welds were 605 µm, 639.5 µm, and 594.4 µm, respectively. As the lower sheet thickness was 1.1 mm, the penetration depths indicated that all welds were good obtained using the laser power and welding speed combinations listed in Table 3. Additionally, as per recommendations from automotive manufactures (both original equipment manufacturers and Tier 1 suppliers), the minimum requirements for the throat thickness and leg length should be greater than 0.7 times the thickness of the top sheet and 0.9 times the minimum sheet thickness (i.e. throat thickness $\geq 0.7*t_{top}$ and leg length $\geq 0.9*t_{min}$), respectively. The average values of throat thickness were 847.9 µm, 975.1 µm, and 952.4 µm for 0.2 mm,

0.4 mm and 0.6 mm gap-bridged fillet edge welds which satisfied the minimum recommended requirements for the throat thickness. Similarly, much higher values were obtained for the average leg length for the three part-to-part gaps which were 1828.6 µm, 2084 µm, and 1757 µm for 0.2 mm, 0.4 mm and 0.6 mm gap-bridged fillet edge welds, respectively. Therefore, all the three joints were in the good-weld category and further used for high rate and temperature characterisation.

The middle value of part-to-part gaps (i.e. 0.4 mm) was chosen as a representative joint for further microstructural-crystallographic characterisation and micro-hardness analysis as other two gap values were either considered extreme cases with respect to the gap. The EBSD image provided vital information on the fusion zone grain distribution and formation of grains from base material to the fusion zone. The crystallographic orientation of grains from the 0.4 mm gap-bridged fillet edge weld is shown in Figure 7.

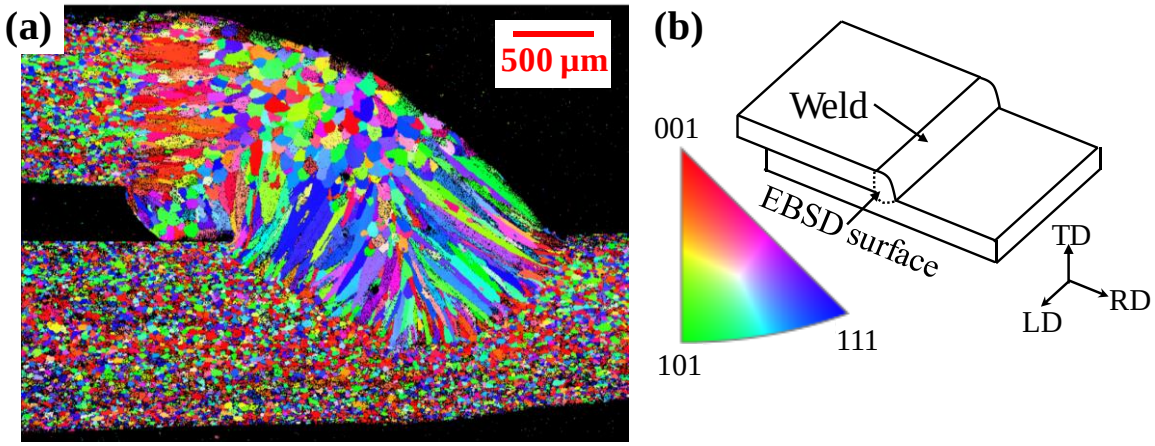

Figure 7 (a) EBSD maps of 0.4 mm gap-bridged filet edge weld showing the grain formation and distribution, and (b) unit triangle and schematic geometry of EBSD surface about rolling direction (RD), transverse direction (TD) and longitudinal direction (LD).

The fusion zone was inspected in a plane normal to the longitudinal direction (LD) as per schematic in Figure 7(b). The crystallographic orientation map obtained from the EBSD result represents the details of grain size distribution and their orientation across the weld zone (i.e. from the base material to fusion zone). A distinct boundary was observed in between the

base material and fusion zone where a sharp change in grain size was noticed. The inverse pole map, as shown in Figure 7(a), reveals the columnar grain formation from base material to the centre of the weld. With respect to the crystallographic orientation, the fusion zone can be divided into three areas: (i) mostly elongated horizontal grains originating from the upper part primarily with 001 orientation and as long as 400 µm, (ii) grains originating from the inner side of the lower part aligned vertically and having grain orientations mostly of 111 and 101 and as long as 700 µm, and (iii) comparatively smaller equiaxed grains (i.e. average grain size of 80 µm) formed between the horizontal and vertical columnar grains with a mixture of different crystallographic orientations. These grain orientation and columnar formations were the results of the directional cooling of the fusion zone where heat was mainly conducted away from the molten material to the base material [14].

Similarly, the microhardness profile measured for 0.4 mm gap-bridged fillet edge weld provided insightful distribution of microhardness from upper base material to fusion zone and lower base material. Figure 8(a) shows the mapping of microhardness values with respect to the actual position on the welded geometry. It was observed that fusion zone microhardness values were lower compared to the base material mainly due to solubilisation of the precipitates and larger grain formation. It is well known, that the material hardness is closely related to the grain size according to Hall-Patch principle, however, Sun, et al. [53] mentioned that the Hall-Petch effect in aluminium alloys was relatively weak compared to precipitation hardening and larger grain formation did not result in a large contribution to the hardness loss of the fusion zone and neighbouring area. The 6xxx series aluminium alloys are mainly precipitation hardened (heat-treated). Therefore, the main strength is coming from the precipitate growth under controlled heating (ageing) to the desired temper state. Figure 8(b) shows the precipitate within the base material whereas Figure 8(c) demonstrates that precipitates have mostly disappeared from the fusion zone.

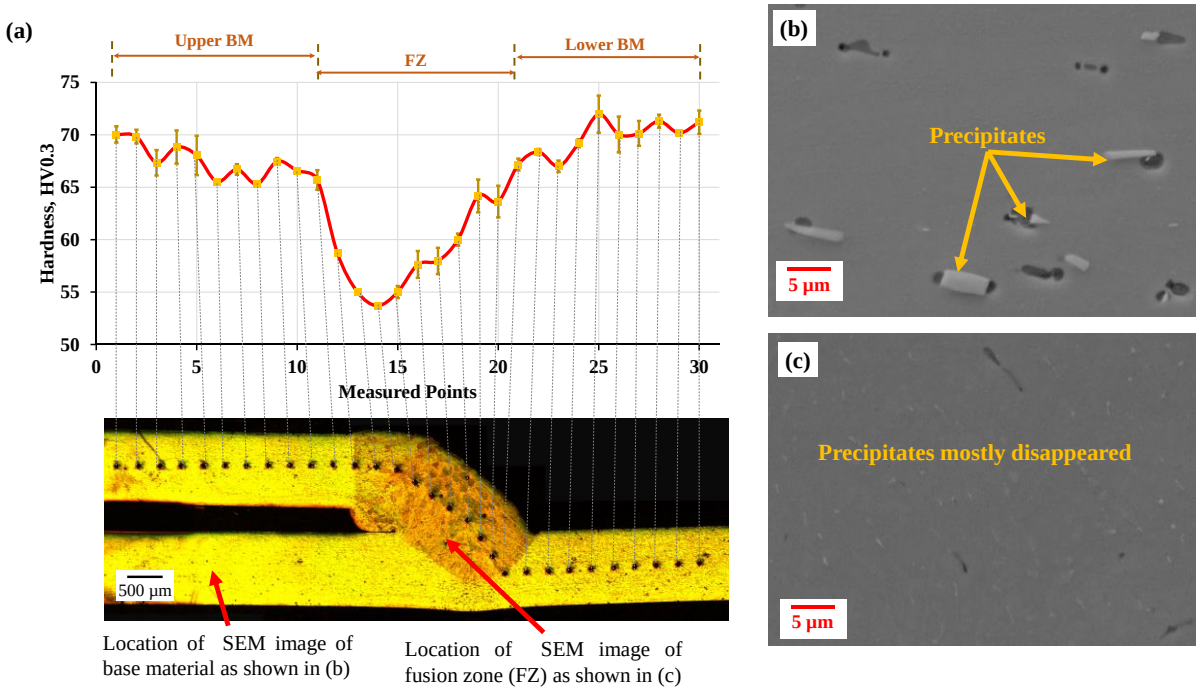

Figure 8 (a) Microhardness profile of 0.4 mm gap-bridged fillet edge weld, (b) – (c) SEM images of base material and fusion zone demonstrating the disappearance of precipitates.

The average hardness value measured for the BM was 68 $HV_{0.3}$ with an observed range of 65 -73 $HV_{0.3}$. Three repeat measurements were conducted each with a total of 30 indents equally spaced within the upper BM, FZ and lower BM. While traversing from the upper BM to the FZ, it was observed that the average microhardness decreased by 10-13 $HV_{0.3}$. Thereafter, the microhardness started to increase when moving to the centre of the weld bead. Subsequently, the hardness value again increased in the boundary region of the fusion zone and lower sheet base material. It can be seen from Figure 8(a) that there is some fluctuation in microhardness values within the FZ which can be attributed to (i) variation during the welding process where it was difficult to obtain a homogeneous mixture, and (ii) grain size distribution, grain orientation, and crystallographic direction [52, 54] as a result of directional cooling. Additionally, slight microhardness fluctuation was observed within the base material before entering the fusion zone and after leaving the fusion zone in the first few millimetres and is possibly due to exposure to elevated heat during the welding, release of internal stresses and

thermal softening [55-57]. As a result, over ageing took place during welding which is common for 6xxx series aluminium alloys [37]. It should be noted that being an autogenous process, RLW does not use external material (such as filler wire or powder) during the welding process and the same parent material was melted and fused to form the fusion zone. The main hardness drop can be attributed to the disappearance of the precipitates as shown in Figure 8(b)-(c), larger columnar grain formation, and localised hardness due to fusion zone grain variation [9].

3.3. High-rate characterisation of gap-bridged RLW fillet edge welds

High-speed test data (i.e. the load-displacement curves) is generally noisy due to inertia effects of the system [48]. To remove noise from the test data, a two-stage filtering method, as recommended for filtering high-rate data [46, 48], was applied where (i) the high-frequency noise was eliminated by using a Butterworth filter with 1 kHz cut-off frequency, and then (ii) the low-frequency noise was smoothed using a moving average filter. For example, Figure 9(a) shows the unfiltered and filtered load-displacement curves obtained from the 0.4 mm gap-bridged fillet edge weld tested at 5.0 m/s. Three specimens were tested for each part-to-part gap condition (i.e. 0.2 mm, 0.4 mm and 0.6 mm) at four dynamic test speeds (i.e. 0.1, 1.0, 5.0 and 10.0 m/s). Figure 9(b) shows the load-displacement curves obtained from the three repeat tests of 0.4 mm gap-bridged RLW fillet edge weld at 5.0 m/s. The average load-displacement behaviour was obtained for each speed and part-to-part gap combination for analysis.

The typical deformation sequences from the high-speed digital camera recordings of a 0.4 mm gap-bridged RLW fillet edge weld lap shear specimen tested at 5.0 m/s are shown in Figure 10. A total of eight slide images are shown starting from the unloaded condition until failure. Predominantly, the failure location was observed near the junction of upper part base material and fusion zone (i.e. HAZ or nearby) for all test speeds and part-to-part gap conditions. There was no visible evidence of another failure mode in all the lap shear specimens tested.

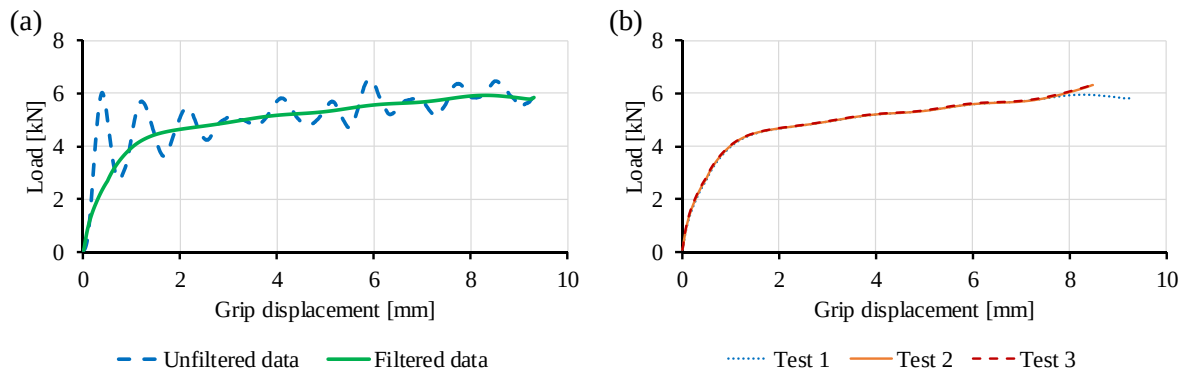

Figure 9 (a) Unfiltered and filtered load-displacement curves obtained from 0.4 mm gap-bridged fillet edge weld test at 5.0 m/s, and (b) load-displacement curves obtained from the repeat tests of 0.4 mm gap-bridged fillet edge welds at 5.0 m/s.

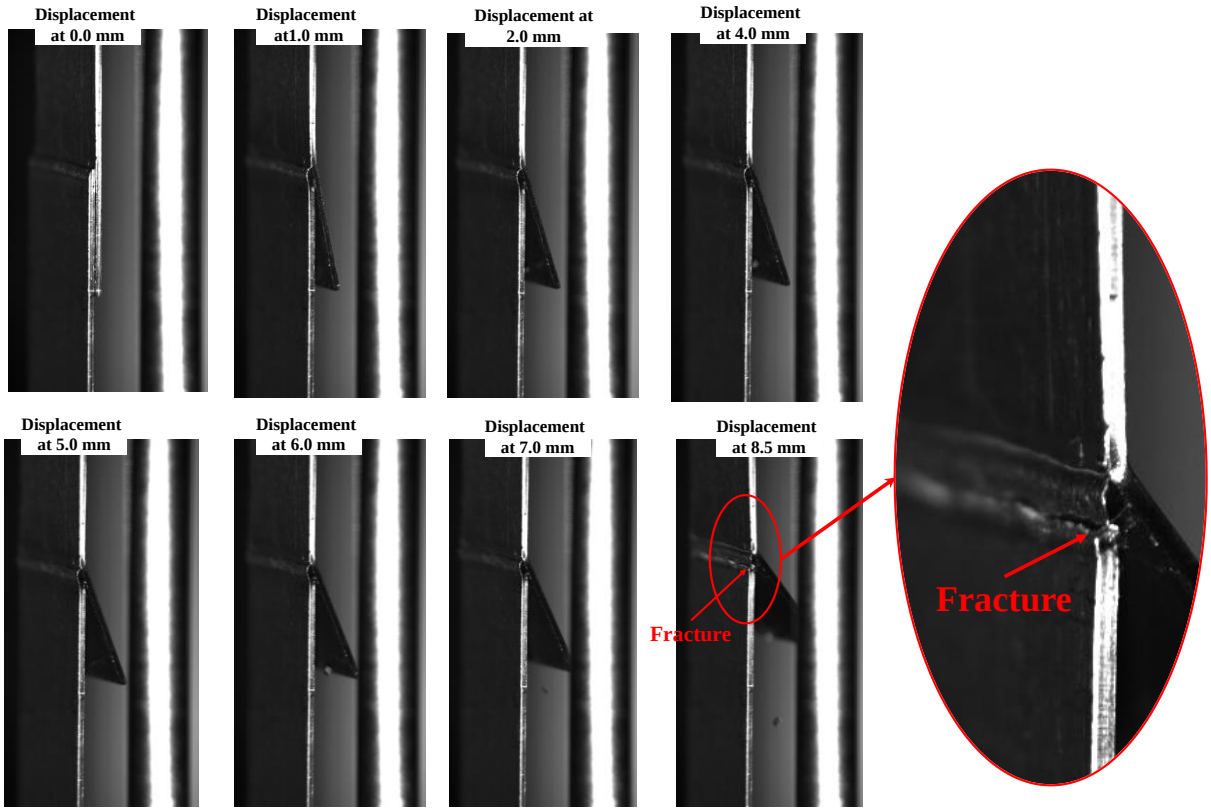

Figure 10 High-speed digital camera recordings of the typical deformation sequences of the 0.4 mm gap-bridged RLW fillet edge weld tested at 5.0 m/s.

Due to the nature of the lap shear sample, as shown in Figure 10, the deformation is not symmetric. The lower overlap part was bent away from the upper part making the fusion zone a hinge point. After starting the lap shear test, the fusion zone slowly rotated to become aligned

with the upper and lower parts where the load was transmitted through the fusion zone to the upper and lower parts. With the increase in grip displacement, the experienced load and subsequent elongation within the fusion zone were increased. Due to the elongation of the fusion zone and the slight rotation, the lower overlap part started to bend. With the increase in experienced load, the lower overlap part, which was not in line with the load application, bent further away from the upper part and eventually leading to the fracture. These non-symmetric modes of deformation and failure were consistent for all the lap shear specimens tested across all speed and part-to-part gap combinations.

The average load-displacement curves obtained from three part-to-part gap-bridged fillet edge welds tested at 0.1 m/s, 1.0 m/s, 5.0 m/s and 10.0 m/s are plotted in Figure 11. Maximum mean load and maximum mean grip displacement to failure were considered as the weld quality performance measures for high-rate characterisation. In general, a slight increment in maximum mean load to failure was observed accompanied by minor or no increment in maximum mean grip displacement with increasing test speed. These values are listed in Figure 11 (d) with associated standard errors. Similar to these results, low strain rate sensitivity was reported in the literature for aluminium alloys during parent material testing [27] whereas self-piercing riveting joints of AA5754 alloy exhibited low strain rate sensitivity over a test rate range from low (10^{-3} m/s) to high (5.0 m/s) [48]. However, in the case of RLW gap-bridged fillet edge welds, a small increment in load was observed with increasing test speed together with an increment in mean grip displacement to failure. For example, around 6.6%, 3.5% and 7.7% incremental change in maximum mean load to failure was observed for 0.2 mm, 0.4 mm and 0.6 mm gap-bridged fillet edge welds respectively when the test speed was increased from 0.1 m/s to 1.0 m/s. In contrast, relatively larger change (around 20 – 30% increase) in maximum mean grip displacement to failure was observed when the test speed was increased from 0.1 m/s to 1.0 m/s for all gap conditions. Therefore, the ductility and peak strength of the RLW

samples were increased with the test speed from 0.1 m/s to 1.0 m/s. In general, the main difference in mechanical behaviours from static to dynamic testing can be attributed to the activation of different slip systems, differences in dislocation mobility, pile up and accommodation processes under different strain rates [58, 59]. Furthermore, the increased ductility of the RLW joint sample can be attributed to the inertia effects of the whole sample geometry. For example, RLW joints tested at a slower rate were allowed more time to deform before the final fracture occurred at the joint region and resulted in a slower deformation rate. Due to this slower deformation rate, the fracture can propagate quickly at failure load and displacement. In contrast, at higher test speed, higher deformation rate accompanied by the sample inertia resulted in larger mean grip displacement and maximum load at failure before fracture criteria were activated. However, at much higher rates (i.e. 5.0 m/s and 10.0 m/s), the maximum mean load, as well as maximum mean grip displacement to failure, exhibited no clear trend. A similar observation was made by Sun and Khaleel [50] where they reported that the strength increase from 4.47 m/s (10 mph) to 8.94 m/s (20 mph) is not as significant as the strength increase from static to 4.47 m/s when they tested self-piercing rivets (SPR) and resistance spot welds (RSWs). In particular, resistance spot welded aluminium exhibited increasing joint strength with increasing test speed, however, the strength increase at higher rate was not as significant compared to the strength increase from static to moderate speed. However, they found that with increasing loading velocity, mean displacement to failure decreased for all the self-piercing rivets (SPR) and resistance spot welds (RSWs) which contradicts the finding from this RLW joint investigation. Therefore, it may be suggested that the ductile behaviour and variation at higher rates were the result of the higher deformation rate accompanied by the sample inertia, variation within the RLW process, variations coming from the test procedure, the change in flow stress, dynamic recovery or adiabatic heating effect at higher rates [29, 60].

Furthermore, it can be observed that the average maximum load obtained from all three part-to-part gap conditions were similar. Being a non-contact joining process, it is considered difficult to compensate for part-to-part gaps with RLW as often discontinuous joints may be achieved without appropriate fusion geometry at higher gaps. Therefore, it is expected that higher part-to-part gap values may result in inferior quality welds having lower average mean load and average grip displacement to failure in comparison with low gap values. This phenomenon may be attributed to the size of the fusion zone. An overall good contact of the fusion zone to the lower base material may not be achieved with higher gaps and result in lower penetration values [14]. However, the results obtained in this study demonstrate that a good quality weld can be achieved by bridging the part-to-part gaps using appropriate RLW process parameters. The cross-sectional images in Figure 6 show that similar penetration depth can be achieved even with increasing part-to-part gaps.

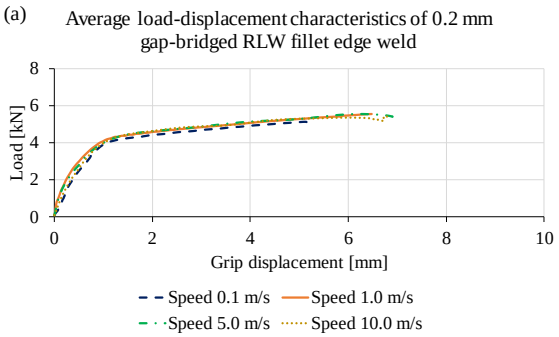

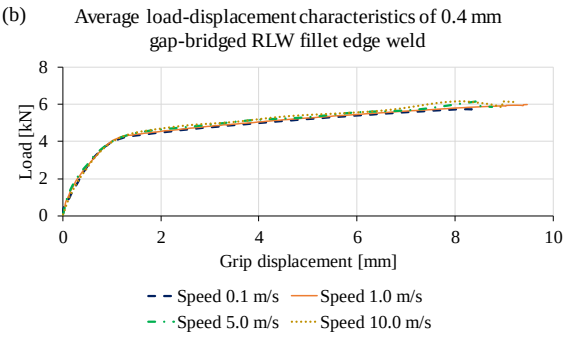

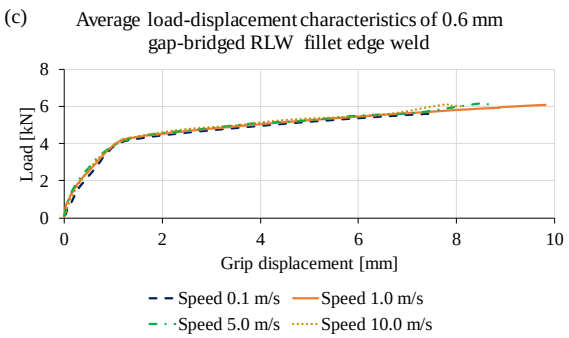

Test speed [m/s]	Part-to-part gap					
	0.2 mm gap		0.4 mm gap		0.6 mm gap	
	Maximum mean load [kN]	Maximum mean grip displacement [mm]	Maximum mean load [kN]	Maximum mean grip displacement [mm]	Maximum mean load [kN]	Maximum mean grip displacement [mm]
0.1	5.15 ±0.02	5.25 ±0.06	5.76 ±0.03	8.35 ±0.01	5.60 ±0.03	7.56 ±0.17
1.0	5.49 ±0.06	6.23 ±0.55	5.96 ±0.04	9.47 ±0.28	6.03 ±0.09	9.82 ±0.51
5.0	5.54 ±0.01	7.07 ±0.09	6.19 ±0.13	8.75 ±0.27	6.18 ±0.02	8.64 ±0.02
10.0	5.39 ±0.03	6.85 ±0.23	6.17 ±0.04	9.21 ±0.59	6.05 ±0.09	8.09 ±0.57

Figure 11 Load-displacement curves from lap shear tests at various test speeds for (a) 0.2 mm gap, (b) 0.4 mm gap, (c) 0.6 mm gap-bridged fillet edge welds, and (d) maximum mean load and maximum mean grip displacement to fracture obtained from the three gap conditions.

3.4. Deformation and strain distribution using DIC

Digital image-based strain distribution measurement [51] at various tensile rates provides information about the deformation process and local strain distribution near the weld area [49]. Figure 12 shows the aspect of axial deformation and strain distribution across the weld region with selected sequences of strain mapping (at different tensile stages obtained from DIC), for example, (a) the 0.4 mm RLW gap-bridged AC-170PX fillet edge joint tested at the tensile rate of 1.0 m/s, and (b) the 0.2 mm RLW gap-bridged AC-170PX fillet edge joint tested at the tensile rate of 10.0 m/s. The strain distribution curve can be divided into two distinguished regions, namely, the elastic increment, and then, the plastic increment. For example, taking the results of 0.4 mm gap-bridged RLW fillet edge weld tested at 1.0 m/s, see Figure 12(a), it was observed that the specimen started to deform uniformly after loading at the beginning, and shortly after, strain localisation started to appear. This phenomenon can be attributed to the nature of the lap shear sample where the lower overlap part was bent away from the upper part making the fusion zone a hinge point where the strain was started to localise. In addition, the FZ strength was relatively weaker compared to the base material [14] and the location of the failure was generally within the welded region nearer the upper base material. Strain localisation was started to develop within 0.72 ms for 0.4 mm gap-bridged sample tested at 1.0 m/s and a strain value of 0.11 at 0.9 ms was measured as the start of the plastic increment. The strain value gradually increased with time and the failure strain was recorded as 0.23 at 9.0 ms. In the parent material testing, the typical strain behaviour caused by increasing loading starts with uniform strain distribution over the specimen length and finally ends with localized necking [49] which can be interpreted as the point at which load reached the maximum (i.e. UTS) and then started to drop during necking with the failure at the end. However, in case of RLW fillet edge weld, joint failure was obtained at the maximum load, hence, the diffuse necking might result in localised strain formation but the localised necking was not clearly

observed. The strain started to develop across the weld region and increased until failure. These contours of the inhomogeneous strain distinctly suggest that strain localisation in the form of diffuse necking has already started at very early stages.

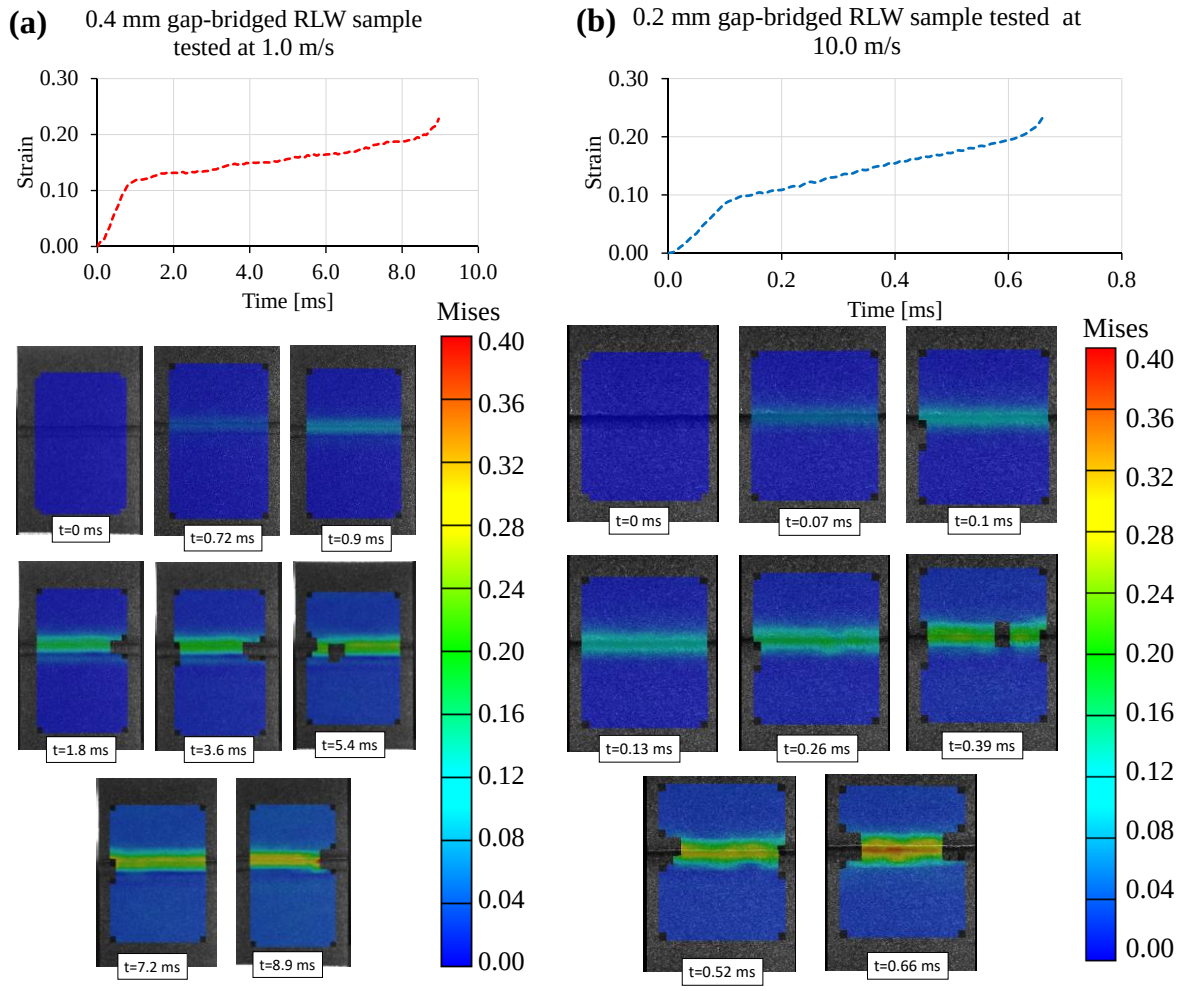

Figure 12 DIC based strain measurement examples with sequences of the high-speed digital images and associated strain maps for (a) 0.4 mm gap-bridged RLW fillet edge weld tested at 1.0 m/s, and (b) 0.2 mm gap-bridged RLW fillet edge weld tested at 10.0 m/s.

Similarly, in case of 0.2 mm gap-bridged RLW fillet edge weld specimen tested at 10.0 m/s, see Figure 12(b), strain localisation was observed at a very early stage at approximately 0.07 ms and thus strain localisation started even before the time point of the elastic to plastic increment (i.e. at 0.1 ms). The failure strain was obtained as 0.23 at 0.7 ms. Therefore, six representative deformation stages from unloaded specimen until the onset of failure are

selected and displayed in Figure 12. The results suggest that the strain had already started to localise before reaching the intersection of elastic and plastic increments due to (i) the FZ acted as hinge point of the asymmetric lap shear sample, and (ii) slightly low FZ strength compared to BM. Only using the deformed geometries and the stress-strain curve, this strain localisation phenomenon could not be determined. High-speed imaging-based DIC method delivered useful observations of the start of diffuse necking and the strain fields in the localised zone of the gap-bridged RLW fillet edge welds at high-rates.

The results from all the test speeds (i.e. 0.1 m/s, 1.0 m/s, 5.0 m/s and 10.0 m/s) and all part-to-part gaps (i.e. 0.2 mm, 0.4 mm and 0.6 mm) were similar with respect to the strain localisation phenomenon. Additionally, the strain field maps indicated that the strain localisation always happened across the weld region. Typically, the strain distribution curve was started by increasing load with strain localisation at the joint and elastic extension of the overall specimen, finally ending with localised abrupt facture /peeling along the joint seam. No significant change in fracture strain was observed due to the effect of test speed variation. The measured fracture strain from different gaps and test speeds range between 0.21 to 0.25.

3.5. Elevated and depressed temperature responses

The RLW gap-bridged test specimens for all the gap conditions were tested at six levels of temperature of which two were at depressed (i.e. -50°C and 0°C) and four were at elevated temperature (i.e. 50°C, 100°C, 200°C, and 300°C). The average load-displacement curves obtained from all three gap-bridged RLW fillet welds at varying temperatures are plotted in Figure 13(a)-(c). The maximum mean loads and maximum mean grip displacements with associated standard errors are tabulated in Figure 13(d).

In general, aluminium alloy exhibit higher yield strength, tensile strength and elongation at failure at a lower temperature [61]. Consistent with this behaviour, all the RLW gap-bridged fillet edge welds tested at -50° exhibited the highest maximum load and grip displacement

compared to the other temperatures. In addition, due to incremental change in flow stress at low temperature, the load-displacement curve followed a higher deformation path due to higher flow stress-strain behaviour. For example, in the case of the 0.2 mm gap-bridged fillet edge weld, a maximum load to failure of 5.91 kN at a grip displacement of 10.15 mm was obtained.

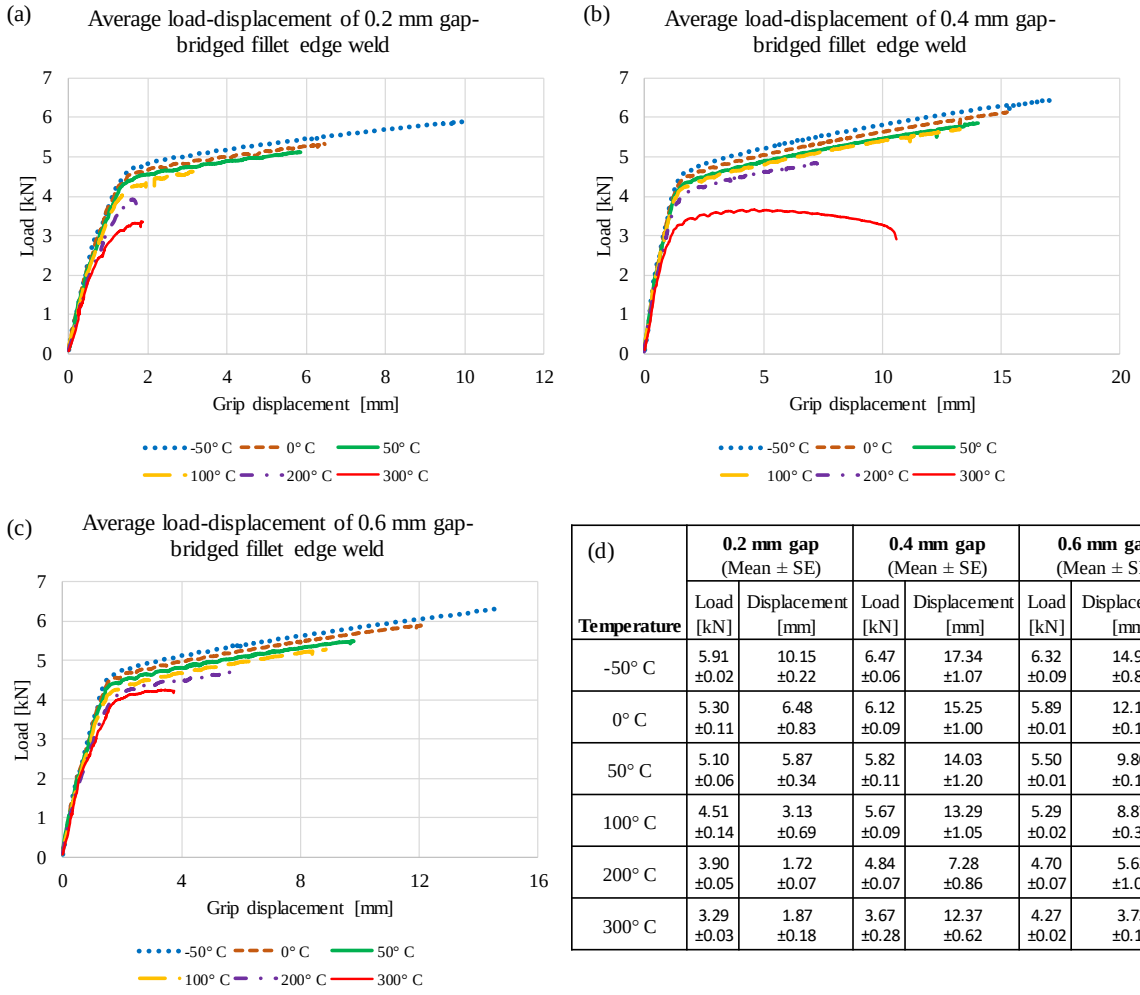

(d)

Temperature	0.2 mm gap (Mean ± SE)		0.4 mm gap (Mean ± SE)		0.6 mm gap (Mean ± SE)	
	Load [kN]	Displacement [mm]	Load [kN]	Displacement [mm]	Load [kN]	Displacement [mm]
-50° C	5.91 ±0.02	10.15 ±0.22	6.47 ±0.06	17.34 ±1.07	6.32 ±0.09	14.94 ±0.80
0° C	5.30 ±0.11	6.48 ±0.83	6.12 ±0.09	15.25 ±1.00	5.89 ±0.01	12.16 ±0.13
50° C	5.10 ±0.06	5.87 ±0.34	5.82 ±0.11	14.03 ±1.20	5.50 ±0.01	9.80 ±0.14
100° C	4.51 ±0.14	3.13 ±0.69	5.67 ±0.09	13.29 ±1.05	5.29 ±0.02	8.87 ±0.30
200° C	3.90 ±0.05	1.72 ±0.07	4.84 ±0.07	7.28 ±0.86	4.70 ±0.07	5.63 ±1.01
300° C	3.29 ±0.03	1.87 ±0.18	3.67 ±0.28	12.37 ±0.62	4.27 ±0.02	3.73 ±0.19

Figure 13 Load-displacement curves at depressed and elevated temperatures from (a) 0.2 mm, (b) 0.4 mm, (c) 0.6 mm gap-bridged fillet edge welds, and (d) maximum mean load and corresponding mean displacements with associated standard errors.

With an increase in temperature, both the maximum load at failure and corresponding displacement gradually reduced without a significant reduction in yield strength up to 100°C. For example, the maximum load gradually dropped to 5.30 kN, 5.10 kN and 4.51 kN with corresponding grip displacements of 6.48 mm, 5.87 mm and 3.13 mm when the 0.2 mm gap-

bridged RLW fillet edge weld samples were tested at 0°C, 50°C and 100°C respectively. More consistent drops in both maximum load and maximum grip displacement at failure were recorded (i.e. an average of 4.5% drops in maximum load and 9.3 % drops in grip displacement at failure) for 0.4 mm gap-bridged RLW specimens when temperature gradually increased from -50°C to 100°C. Similar load-displacement behaviours were observed for the 0.6 mm gap-bridged RLW fillet edge welds as shown in Figure 13(c) when specimens were tested at temperatures between -50°C to 100°C. Further increase in temperature had a severely detrimental effect on the physical properties of aluminium alloys. This mechanical property degradation at elevated temperature can in part be understood through the strengthening mechanisms. Generally, 6xxx-series aluminium alloys are precipitation hardened (heat-treated) where the primary strengthening mechanism is through precipitate growth under controlled heating (ageing) to the desired temper state [62]. However, further exposure to elevated temperature accelerates precipitate growth causing over-ageing and subsequently, strength reduction. Langhelle and Amdahl [63] found that property degradation of aluminium alloys occurred at temperatures as low as 150°C and around 50% yield strength reduction was observed at ~275°C. A gradual loss of yield strength was observed at and beyond 200°C, accompanied with a reduction in maximum load and displacement at failure, as the flow stress was considerably decreased with the increase in temperature [32, 36]. A similar observation was reported by Summers, et al. [32] when 5083-H116 aluminium alloy was tested between 200°C – 350°C. At the temperatures of 200°C and 300°C, the maximum mean load at failure was 3.90 kN and 3.29 kN respectively for the 0.2 mm gap-bridged specimens and similar observations were obtained from the other two part-to-part gap conditions. The only anomaly obtained in failure mode was for 0.4 mm gap-bridged specimen tested at 300°C where the failure mode was the parent material rather than the joint. As mentioned earlier, the typical mode of joint failure was a fracture of the upper part near the junction of the base material and

fusion zone. However, while testing the 0.4 mm gap-bridged joints at 300°C, the joint actually appeared to be stronger than the base material. Due to these reasons, a higher grip displacement of 12.37 mm was obtained for 0.4 mm gap-bridged joints at 300°C while 1.87 mm and 3.73 mm were the average grip displacements to failure from the 0.2 mm and 0.6 mm gap-bridged RLW fillet edge welds.

4. Constitutive modelling to represent RLW gap-bridged joints

The commercial finite element software LS-Dyna was used for modelling the deformation behaviour of gap-bridged RLW fillet edge welds. Based on the fusion zone geometry obtained from the three gap-bridged RLW fillet edge welds, finite element models were developed for the different gap conditions. Solid elements give more accurate results in comparison with shell elements as they are more suitable to calculate stress in all the three directions. Therefore, a solid cubic mesh was chosen to represent the weld zone which also can easily represent the part-to-part gaps. An initial element size sensitivity study was conducted and based on this, uniform element size was selected to represent all the three gap-bridged fillet edge weld configurations. The basic element size was within 0.1-0.2 mm. The mesh model of the test specimens with subsections and other elements included in the model are shown in Figure 14(a) where the model is composed of the fusion zone (i.e. weld), upper part, lower part, static grip, moving grip, elastic spring and loading direction (represented with red arrows). The mesh models of 0.2 mm, 0.4 mm, and 0.6 mm gap-bridged fusion zones are shown in Figure 14(b)-(d), respectively. To capture the experienced load during the lap shear tests, the elastic spring was attached to the static grip section and it emulated the load-cell of the VHS test equipment. The spring stiffness plays an essential role in avoiding the initial noise in the recorded data. The stiffness of the elastic spring was set at 100,000 N/m to remove the unwanted noise from the load. Additionally, a smooth load sequence (i.e. a small acceleration time to reach the

required velocity and then constant velocity for the rest of the test) was applied to remove the initial loading noise. The static grip and moving grip were modelled as rigid bodies.

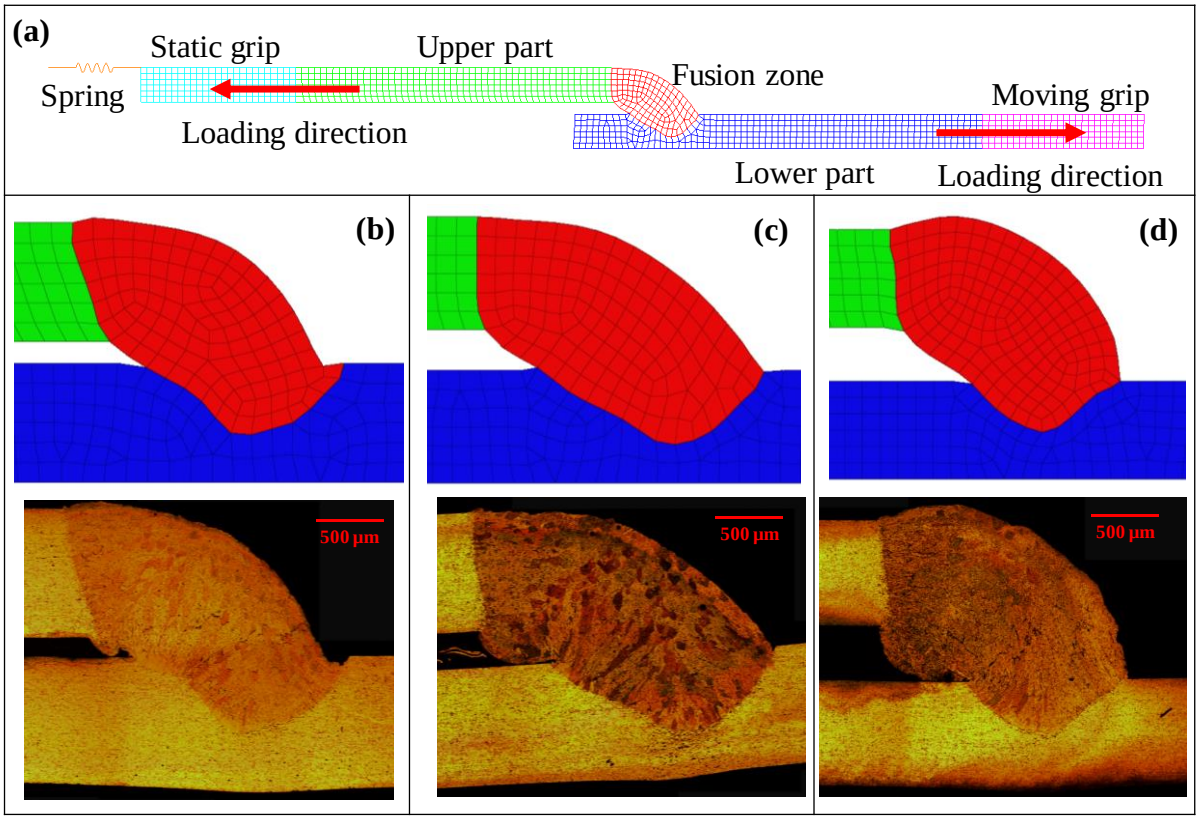

Figure 14 Schematic of finite element mesh model set-up of lap shear test specimen (a) representative test specimen, and (b) – (d) fusion zones of 0.2 mm, 0.4 mm and 0.6 mm gap-bridged RLW fillet edge welds, respectively.

Typically, high-rate plastic deformation of materials can be described by a number of constitutive equations which basically express the stress as a function of strain, strain rate and temperature. Therefore, stress can be represented as the following:

$$stress, \sigma = f(\varepsilon, \dot{\varepsilon}, T) \quad (1)$$

where $\varepsilon, \dot{\varepsilon}, T$ denote the strain, strain rate and temperature respectively.

Several constitutive models have been proposed to describe the plastic behaviour of materials to address the dependence on the stain, strain rate and temperature. One widely used empirical model, the Johnson-Cook (J-C) model, considers the effects of isotropic (static) strengthening,

kinematic strengthening, temperature variation and the associated variation in yield strength [34, 64]. The flow stress in the J-C model [65] is determined as

$$\sigma = (A + B\varepsilon^n)(1 + C\ln \dot{\varepsilon}^*)\left(1 - \left(\frac{T-T_r}{T_M-T_r}\right)^m\right) \quad (2)$$

where the term $(A + B\varepsilon^n)$ represents the parabolic work hardening at low strain rates in terms of yield stress (A), strain hardening effect (B), strain rate constant (n) and equivalent plastic strain (ε). The term $(1 + C\ln \dot{\varepsilon}^*)$ is the contribution due to high strain rate dependency based on the strain rate constant (C) and the dimensionless plastic strain rate ($\dot{\varepsilon}^* = \dot{\varepsilon}/\dot{\varepsilon}_0$, in which $\dot{\varepsilon}_0$ is the reference strain rate). The thermal softening effect is calculated as $\left(1 - \left(\frac{T-T_r}{T_M-T_r}\right)^m\right)$ using room temperature (T_r), melting point temperature (T_M), the temperature of a material element (T) and thermal softening factor (m). Therefore, first, second and third terms in the J-C model (as in eq. 2) represents the strain, strain rate and temperature, respectively. In the case of low strain rate sensitivity, the constitutive expression can be shortened to

$$\sigma = (A + B\varepsilon^n)\left(1 - \left(\frac{T-T_r}{T_M-T_r}\right)^m\right) \quad (3)$$

These equations are incorporated in the MAT_224, the tabulated J-C material model [66] where the relation between stress vs strain with respect to temperature can be represented in tabulated curves. The flow stress (σ) in the tabulated J-C material model is represented as

$$\sigma_y = k_1(\varepsilon)\frac{k_t(\varepsilon,T)}{k_t(\varepsilon,T_r)} \quad (4)$$

where, $k_1$and k_t are the load curves or tables corresponding to plastic strain and temperature dependent plastic strain responses respectively. With the general tabulated input parameters, the temperature dependent behaviour can be simulated.

The tabulated J-C model was used in this study to assign the material properties of the base material as well as the weld fusion zone. Fully integrated elements were selected to remove the hourglass effect (i.e. localised excess distortion within the elements). Additionally, a fusion zone scale factor (i.e. ratio of fusion zone strength to base material strength) and

localised fracture strain are equally important to simulate the identical failure location and failure mode observed in the test. For example, the result obtained from 0.4 mm gap-bridged fillet edge weld at room temperature is shown in Figure 15. The load-displacement curves from the simulation as plotted in Figure 15(a) shows a close agreement with the test data. The Von-Mises stress plots from the sequence of the simulation stages across the fusion zone are plotted in Figure 15(b) and represent (1) the start of the loading cycle, (2) the end of the elastic region, (3) 4.0 mm grip displacement in the plastic region, (4) 7.0 mm grip displacement in the plastic region, (5) immediately before fracture, and (6) after fracture. The maximum Von Mises stress obtained from the J-C model at room temperature was 260.47 MPa.

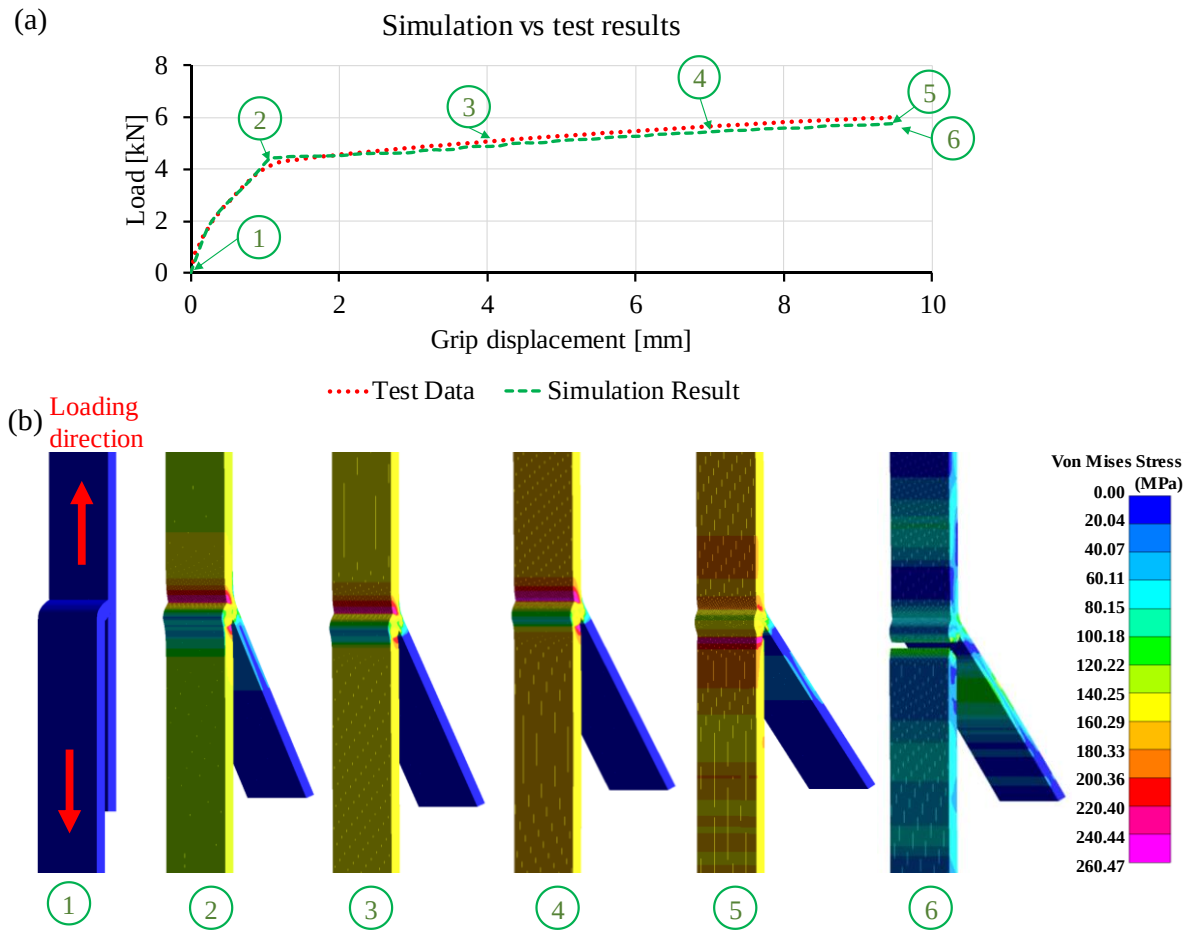

Figure 15 (a) Load-displacement curves from simulation and experimental tests for 0.4 mm gap-bridged fillet edge weld at room temperature tested at 0.1 m/s, and (b) image stages

obtained from simulation to show stress distribution when 0.4 mm gap-bridged fillet edge weld simulated at a rate of 0.1 m/s test.

The depressed and elevated temperature dependent joint behaviours were simulated with changes to the flow curves and fracture strains. There is no significant change in yield strength between -50°C and 100°C and the gap-bridged fillet edge welds exhibit the same load-displacement behaviour, however, fracture strains were gradually decreasing with increasing temperature. As the flow curves changed significantly at 200°C and 300°C, the room temperature flow curve was reverse engineered to simulate the load-displacement characteristics and validated with the test data from RLW fillet edge welds. Therefore, the established tabulated J-C model can effectively predict the experimental test results over a wider range of temperatures. For example, Figure 16 shows a good agreement between the simulated load-displacement curves and test data obtained from depressed temperature (i.e. 0.2 mm gap-bridged RLW joint at -50°C) and elevated temperature (i.e. 0.6 mm gap-bridged RLW joint at 200°C and 300°C). In addition, the image stages obtained from simulation depicts the stress distribution within the base material and fusion zone starting from undeformed geometry until fracture. It was observed that the stress started to develop at the boundary of the fusion zone and base material for both the upper and lower sheets. Due to the reduction in flow stress with increasing temperature, the highest Von Mises stress obtained from the J-C model at fracture also gradually decreased. For example, the maximum stress obtained from the 0.2 mm gap-bridged RLW joint at -50°C was 270.32 MPa while the maximum stresses for the 0.6 mm gap-bridged RLW joint were 199.16 MPa and 185.32 MPa at 200°C and 300°C, respectively.

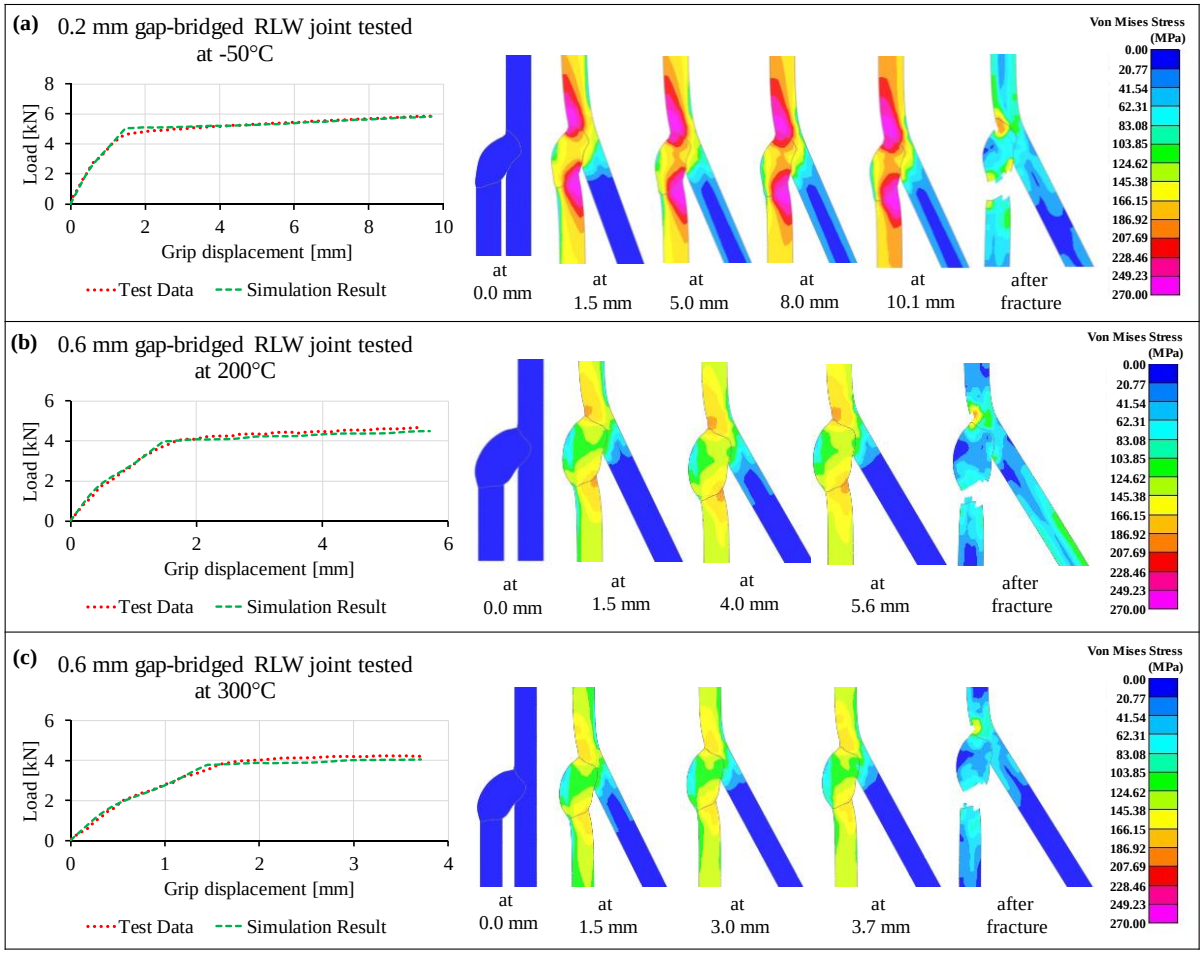

Figure 16 Load-displacement curves and corresponding image stages obtained from simulation to show stress distribution (a) 0.2 mm gap-bridged RLW fillet edge weld tested at -50°C, (b) 0.6 mm gap-bridged RLW fillet edge weld tested at 200°C, and (c) 0.6 mm gap-bridged RLW fillet edge weld tested at 300°C.

5. Comparison with self-piercing riveting (SPR) and resistance spot welding (RSW)

Widely used joining techniques for automotive body-in-white applications, especially for aluminium structures are self-piercing riveting (SPR) and resistance spot welding (RSW) [67, 68]. For joining aluminium alloys, both SPR and RSW joining techniques have several limitations. For example, SPR possesses disadvantages including recyclability (i.e. steel rivets within aluminium structures), weight addition due to additional rivets, not achieving high strength and both sided access required to place an SPR joint. Similarly, RSW is also not suitable due to low bulk resistance with high electrical/thermal conductivities, presence of

oxide layers at the surface necessitating the use of high welding currents, frequent RSW welding tip degradation leading to inconsistency in joint quality and contact-based joining hindering high yields [69, 70]. In contrast, aluminium alloys can be benefited from single-sided, non-contact, fast RLW joining provided it satisfies the mechanical strength criterion. For a comparative study, SPR and RSW lap joints were made by carefully placing the rivet or weld nugget at the centre of the overlap region as shown in Figure 17.

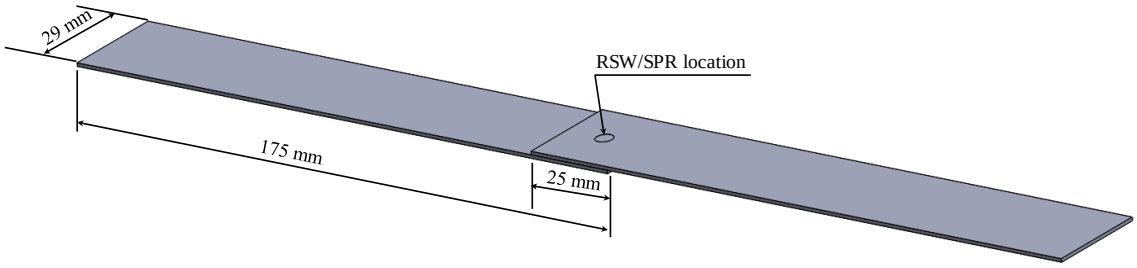

Figure 17 SPR and RSW lap configuration samples with rivet or weld nugget at the centre of the overlap region.

For SPR joining, guidelines and recommendations are available in the literature focusing on process parameters, rivet selection, the profile of die to be used and suitable materials for SPR joining [67, 71, 72]. In this study, the SPR joints were conducted using nominal 5 mm shank diameter hardened steel rivets from the Tucker® SPR system. As per recommendations made by the manufacturers, rivet C5.3 ×5H0 and die M260 416 combinations were used for joining two sheets of AC-170PX of 1.1 mm thickness. Li, et al. [67] concluded that head height is one of the most critical joining parameters for joint strength which can be measured and is the difference between the rivet head and the top sheet surface after producing the joint. In this study, the head height of -0.80 mm was chosen based on the recommendation from the manufacturer as well as relying on the pilot experimentation results.

For RSW joining, the main process parameters reported in the literature are weld current, welding time, sheet thickness and material, the geometry of electrodes, and electrode force applied during the weld [73, 74]. The process parameters used to produce RSW joints in

this study are listed in Table 4 and were obtained from initial screening trials and recommendations from automotive manufacturers. The resistance spot welded test specimens were prepared using a DENGENSHA 100 KVA MFDC Pedestal Spot Welding Machine having a rated capacity of 100 KVA at 50% duty cycle and maximum electrode force of 10 kN. The electrode material used was Z-TRODE® which is an alloy of zirconium and oxygen-free copper.

Table 4 Process parameters used to produce RSW joints using AC-170PX sheets.

Process parameters	Main Weld Current (KA)	Squeeze Time (ms)	Weld Time (ms)	Hold Time (ms)	Electrode Force (kN)	RSW Electrode Tip Face Diameter (mm)
Value	28.0	500	80	300	4.70	M20/R100

As both the SPR and RSW are contact type joining techniques, two-sided access is required to produce the joint and the part-to-part gaps are closed by applying force by either SPR gun or the RSW electrode, respectively. Subsequently, these SPR and RSW joints were compared to the RLW gap-bridged fillet edge welds. Similar to RLW gap-bridged joint testing, three repeats were conducted for both SPR and RSW samples. As low strain rate sensitivity was observed and also reported by Wood, et al. [48], test speed of 0.1 m/s was chosen for this comparative study. The load-displacement characteristics of the SPR and RSW joints are shown in Figure 18 with mean loads and standard errors obtained from the corresponding tests.

No gap SPR and RSW joints are compared with three part-to-part gap-bridged RLW fillet edge welds. Figure 19 shows the mean load from 29 mm long RLW seam weld at different gap conditions against 5 mm diameter SPR joints and approximately 5 mm nugget diameter RSW joints. It was observed that 29 mm RLW stitches on AC-170 PX sheets exhibited average mean loads of 5.15 kN, 5.76 kN and 5.6 kN under 0.2 mm, 0.4 mm and 0.6 mm part-to-part

gap conditions. The average mean loads obtained from the SPR and RSW joints of same material stack-up were 3.34 kN and 2.40 kN, respectively. Under these conditions, it can be concluded that one SPR or RSW joint strength is equivalent to an average of 17.5 mm or 12.7 mm RLW seam, respectively.

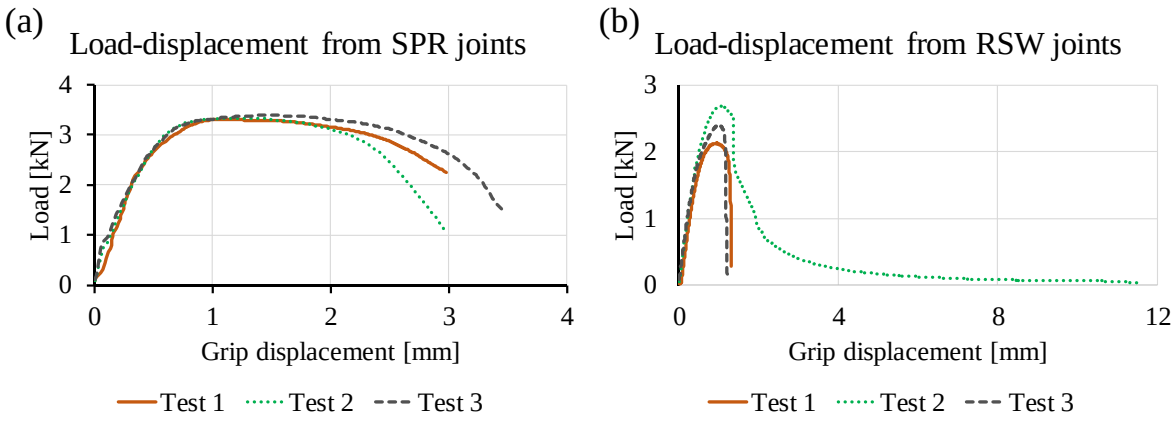

Mean load [kN]	Standard error
3.34	0.024

Mean load [kN]	Standard error
2.40	0.164

Figure 18 Load-displacement curves from lap shear tests at 0.1 m/s test speed from (a) self-piercing revering (SPR), and (b) resistance spot welding (RSW).

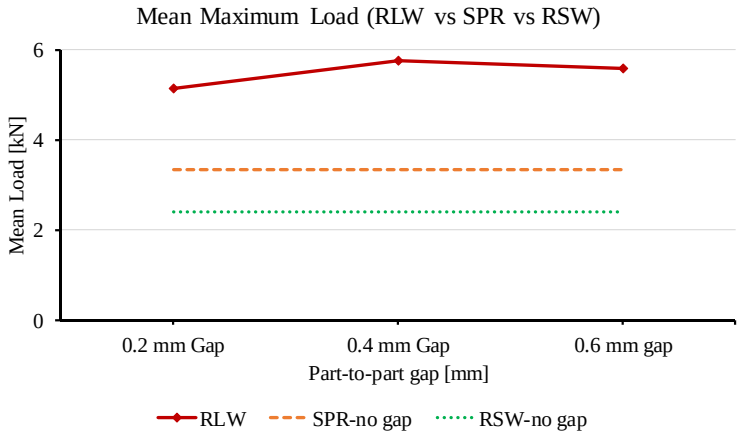

Figure 19 Comparison of mean loads obtained from RLW (29 mm long stitches), SPR (single rivet of 5 mm diameter) and RSW (a single nugget of 5 mm diameter approx.).

6. Conclusions

This paper, for the first time, has explored the behaviour of part-to-part gap-bridged remote laser welded joints under the high-rate and varying temperature conditions using an automotive

grade aluminium alloy AA6014. Three part-to-part gaps (i.e. 0.2 mm, 0.4 mm and 0.6 mm) were successfully bridged by RLW and the fusion zones were examined in details for evaluating the key geometric features (i.e. penetration depth, leg length and throat thickness), grain size distribution and microhardness changes. Based on the results obtained from this study, this paper explores the following areas:

- The merit of the present work is to demonstrate that high quality RLW fillet edge welds could be obtained without using additional material such as filler wire. Furthermore, 'good-weld' characteristics could be achieved by satisfying the key geometric features.
- The fusion zone mainly exhibited columnar grain formations due to the directional cooling. The FZ main hardness drop (around 15-20%) compared to BM can be attributed to the disappearance of precipitates, larger columnar grain, and localised hardness variation.
- The strain rate sensitivity of RLW gap-bridged good-welds is low. Small increments in load were observed with the increasing rate of test speed together with an increase in mean grip displacement at failure.
- The high-speed imaging-based DIC method delivered useful observations on the strain localisation across the weld zone which could not be determined from the load-displacement/stress-strain curves. The average fracture strain measured from the three gap-bridged fillet edge welds at all test speeds were in the range from 0.21 to 0.25.
- This paper has reported a loss of joint strength for all part-to-part gap-bridged RLW welds with increasing temperature due to the decrease in yield strength and flow stress. Thermal softening was the predominant mode of deformation mechanism above 200°C.
- This work successfully demonstrated that the RLW gap-bridged fillet edge welds were equally good for high rate and temperature applications.

- The tabulated J-C model has been shown to effectively predict the RLW joint strength over a wider range of temperatures. This could be of benefit to material and process designers when designing the joints, e.g. to determine the length or location of joints to achieve the desired structural strength for body-in-white or EV battery case applications.
- It was established that gap-bridged RLW could be used to replace both SPR and RSW joints in for automotive applications. An average of 17.5 mm or 12.7 mm RLW seam may be used to replace an SPR or RSW joints, respectively.

Acknowledgements

This research is partially supported by Scansonic IPT GmbH with laser experimental trials. Characterisation and testing were provided by the WMG Centre High Value Manufacturing (HVM) Catapult at The University of Warwick.

Reference

[1] R. Smerd, S. Winkler, C. Salisbury, M. Worswick, D. Lloyd, M. Finn, High strain rate tensile testing of automotive aluminum alloy sheet, International Journal of Impact Engineering 32(1) (2005) 541-560.
[2] W.S. Miller, L. Zhuang, J. Bottema, A.J. Wittebrood, P. De Smet, A. Haszler, A. Vieregge, Recent development in aluminium alloys for the automotive industry, Materials Science and Engineering: A 280(1) (2000) 37-49.
[3] M. Allen, M. Oliveira, S. Hazra, O. Adetoro, A. Das, R. Cardoso, Benchmark 2 – Springback of a Jaguar Land Rover Aluminium, Journal of Physics: Conference Series 734(2) (2016) 022002.
[4] E. Commission, Amending Regulation (EC) No 443/2009 to define the modalities for reaching the 2020 target to reduce CO2 emissions from new passenger cars, Official Journal of the European Union (2014).
[5] U. government, Climate Change Act, Received Royal Assent 26 (2008).
[6] B.G. Pollet, I. Staffell, J.L. Shang, Current status of hybrid, battery and fuel cell electric vehicles: From electrochemistry to market prospects, Electrochimica Acta 84 (2012) 235-249.
[7] A. Das, T.R. Ashwin, A. Barai, Modelling and characterisation of ultrasonic joints for Li-ion batteries to evaluate the impact on electrical resistance and temperature raise, Journal of Energy Storage 22 (2019) 239-248.
[8] J.M. Bergthorson, M.J. Thomson, A review of the combustion and emissions properties of advanced transportation biofuels and their impact on existing and future engines, Renewable and Sustainable Energy Reviews 42 (2015) 1393-1417.
[9] A. Das, I. Butterworth, I. Masters, D. Williams, Evaluation of Key Geometrical and Mechanical Properties for Remote Laser Welded AC-170PX Aluminium Joints, Journal of Laser Micro/Nanoengineering 14(1) (2019) 1-7.
[10] A. Das, D. Li, D. Williams, D. Greenwood, Joining Technologies for Automotive Battery Systems Manufacturing, World Electric Vehicle Journal 9(2) (2018) 22.

[11] M. Kirchhoff, Laser applications in battery production — From cutting foils to welding the case, 2013 3rd International Electric Drives Production Conference (EDPC), 2013, pp. 1-3.
[12] M. Bloeck, Aluminium sheet for automotive applications, Advanced Materials in Automotive Engineering, Woodhead Publishing2012, pp. 85-108.
[13] L. Quintino, R. Miranda, U. Dilthey, D. Iordachescu, M. Banasik, S. Stano, Laser Welding of Structural Aluminium, in: P.M.G.P. Moreira, L.F.M. da Silva, P.M.S.T. de Castro (Eds.), Structural Connections for Lightweight Metallic Structures, Springer Berlin Heidelberg, Berlin, Heidelberg, 2012, pp. 33-57.
[14] A. Das, I. Butterworth, I. Masters, D. Williams, Microstructure and mechanical properties of gap-bridged remote laser welded (RLW) automotive grade AA 5182 joints, Materials Characterization 145 (2018) 697-712.
[15] A. Das, P. Franciosa, A. Pesce, S. Gerbino, Parametric Effect Analysis of Free-form Shape Error during Sheet Metal Forming, International Journal of Engineering Science and Technology 9(09S) (2017) 117-124.
[16] A. Das, P. Franciosa, D. Williams, D. Ceglarek, Physics-driven shape variation modelling at early design stage, Procedia CIRP 41 (2016) 1072-1077.
[17] B. Schleich, N. Anwer, L. Mathieu, S. Wartzack, Skin model shapes: A new paradigm shift for geometric variations modelling in mechanical engineering, Computer-Aided Design 50 (2014) 1-15.
[18] A. Das, P. Franciosa, S. Gerbino, D. Williams, Prediction of Geometric Errors of Stamped Sheet Metal Parts using Deviation Field Decomposition, International Conference on Competitive Manufacturing (COMA), Stellenbosch, South Africa, 2016, pp. 109-114.
[19] A. Das, P. Franciosa, D. Ceglarek, Fixture design optimisation considering production batch of compliant non-ideal sheet metal parts, Procedia Manufacturing 1 (2015) 157-168.
[20] A. Das, Shape variation modelling, analysis and statistical control for assembly system with compliant parts, WMG, University of Warwick, 2016.
[21] P. Fixemer, F. Albert, P. Sievi, T. Graham, Seam Guided Laser Remote Welding with Automated Gap Bridging, Laser Technik Journal 12(2) (2015) 38-41.
[22] F. Albert, P. Marben, T. Graham, Remote Laser Welding of Steel and Aluminum Alloys, Laser Technik Journal 14(1) (2017) 32-35.
[23] A. Alshaer, L. Li, A. Mistry, Understanding the effect of heat input and sheet gap on porosity formation in fillet edge and flange couch laser welding of AC-170PX aluminum alloy for automotive component manufacture, Journal of Manufacturing Science and Engineering 137(2) (2015) 021011.
[24] D. Weller, C. Bezençon, P. Stritt, R. Weber, T. Graf, Remote Laser Welding of Multi-Alloy Aluminum at Close-Edge Position, Physics Procedia 41 (2013) 164-168.
[25] R. Brockmann, C. Bassi, Laser remote welding of aluminum without filler wire, 2012.
[26] L. Djapic Oosterkamp, A. Ivankovic, G. Venizelos, High strain rate properties of selected aluminium alloys, Materials Science and Engineering: A 278(1) (2000) 225-235.
[27] A. Rusinek, J.A. Rodríguez-Martínez, Thermo-viscoplastic constitutive relation for aluminium alloys, modeling of negative strain rate sensitivity and viscous drag effects, Materials & Design 30(10) (2009) 4377-4390.
[28] L. Chen, G. Zhao, J. Yu, Hot deformation behavior and constitutive modeling of homogenized 6026 aluminum alloy, Materials & Design 74 (2015) 25-35.
[29] Y. Chen, A.H. Clausen, O.S. Hopperstad, M. Langseth, Stress–strain behaviour of aluminium alloys at a wide range of strain rates, International Journal of Solids and Structures 46(21) (2009) 3825-3835.
[30] T.R.B. Grandjean, J. Groenewald, J. Marco, The experimental evaluation of lithium ion batteries after flash cryogenic freezing, Journal of Energy Storage 21 (2019) 202-215.
[31] D. Ouyang, M. Chen, Q. Huang, J. Weng, Z. Wang, J. Wang, A review on the thermal hazards of the lithium-ion battery and the corresponding countermeasures, Applied Sciences 9(12) (2019) 2483.
[32] P.T. Summers, Y. Chen, C.M. Rippe, B. Allen, A.P. Mouritz, S.W. Case, B.Y. Lattimer, Overview of aluminum alloy mechanical properties during and after fires, Fire Science Reviews 4(1) (2015) 3.
[33] B.S. Aakash, J. Connors, M.D. Shields, Variability in the thermo-mechanical behavior of structural aluminum, Thin-Walled Structures 144 (2019) 106122.

[34] R. Bobbili, V. Madhu, A.K. Gogia, Tensile behaviour of aluminium 7017 alloy at various temperatures and strain rates, Journal of Materials Research and Technology 5(2) (2016) 190-197.
[35] J.G. Kaufman, Properties of aluminum alloys: tensile, creep, and fatigue data at high and low temperatures, ASM international1999.
[36] H. Hamasaki, Y. Morimitsu, F. Yoshida, Stress relaxation of AA5182-O aluminum alloy sheet at warm temperature, Procedia Engineering 207 (2017) 2405-2410.
[37] M. Pakdil, G. Çam, M. Koçak, S. Erim, Microstructural and mechanical characterization of laser beam welded AA6056 Al-alloy, Materials Science and Engineering: A 528(24) (2011) 7350-7356.
[38] C. Roos, M. Schmidt, Remote Laser Welding of Zinc Coated Steel Sheets in an Edge Lap Configuration with Zero Gap, Physics Procedia 56 (2014) 535-544.
[39] A. Müller, S.-F. Goecke, P. Sievi, F. Albert, M. Rethmeier, Laser Beam Oscillation Strategies for Fillet Welds in Lap Joints, Physics Procedia 56 (2014) 458-466.
[40] A.W. Alshaer, L. Li, A. Mistry, Effect of filler wire properties on porosity formation in laser welding of AC-170PX aluminium alloy for lightweight automotive component manufacture, Proceedings of the Institution of Mechanical Engineers, Part B: Journal of Engineering Manufacture 231(6) (2015) 994-1006.
[41] J. Liu, Novelis Aluminium New Progresses in Auto BiW Lightweight Applications, Automotive International Congress, 2012.
[42] S. Sun, D. E, The investigation of time-dependent springback for AC170PX aluminum alloy at room temperature, Materials & Design 93 (2016) 118-127.
[43] B.E.I. 527-1, Plastics. Determination of tensile properties. General principles, BSI Standards Publication, 2012.
[44] M. Harooni, F. Kong, B. Carlson, R. Kovacevic, Studying the effect of laser welding parameters on the quality of ZEK100 magnesium alloy sheets in lap joint configuration, ICALEO, Laser Institute of America, Anaheim, CA, 2012, pp. 539-548.
[45] B.E.I. 26203-2, Metallic materials. Tensile testing at high strain rates. Servo-hydraulic and other test systems, BSI Standards Publication, 2011.
[46] P.K.C. Wood, C.A. Schley, R.T. Limited, Strain Rate Testing of Metallic Materials and Their Modeling for Use in CAE Based Automotive Crash Simulation Tools, iSmithers2009.
[47] ESIS, P7-00 ESIS Procedure for dynamic tensile tests. TC5 Subcommittee on Dynamic Testing at Intermediate Strain rates., 2000.
[48] P.K.C. Wood, C.A. Schley, M.A. Williams, A. Rusinek, A model to describe the high rate performance of self-piercing riveted joints in sheet aluminium, Materials & Design 32(4) (2011) 2246-2259.
[49] Y. Liu, D. Dong, L. Wang, X. Chu, P. Wang, M. Jin, Strain rate dependent deformation and failure behavior of laser welded DP780 steel joint under dynamic tensile loading, Materials Science and Engineering: A 627 (2015) 296-305.
[50] X. Sun, M.A. Khaleel, Dynamic strength evaluations for self-piercing rivets and resistance spot welds joining similar and dissimilar metals, International Journal of Impact Engineering 34(10) (2007) 1668-1682.
[51] N. McCormick, J. Lord, Digital Image Correlation, Materials Today 13(12) (2010) 52-54.
[52] S.K. Dinda, M. Basiruddin Sk, G.G. Roy, P. Srirangam, Microstructure and mechanical properties of electron beam welded dissimilar steel to Fe–Al alloy joints, Materials Science and Engineering: A 677 (2016) 182-192.
[53] T. Sun, A.P. Reynolds, M.J. Roy, P.J. Withers, P.B. Prangnell, The effect of shoulder coupling on the residual stress and hardness distribution in AA7050 friction stir butt welds, Materials Science and Engineering: A 735 (2018) 218-227.
[54] G.B. Rathmayr, A. Hohenwarter, R. Pippan, Influence of grain shape and orientation on the mechanical properties of high pressure torsion deformed nickel, Mater Sci Eng A Struct Mater 560(2-3) (2013) 224-231.
[55] F. Liu, B. Zhou, Y. Mao, C. Huang, Y. Chen, Z. Wang, Microstructure and mechanical properties of laser welded joints between 2198/2060 Al–Li alloys, Materials Science and Technology 34(1) (2018) 111-122.

[56] S. Dhara, A. Das, Impact of ultrasonic welding on multi-layered Al–Cu joint for electric vehicle battery applications: A layer-wise microstructural analysis, Materials Science and Engineering: A 791 (2020) 139795.
[57] A. Das, T. Dale, I. Masters, D. Widanage, Feasibility of fillet edge weld using laser wobble technique, Procedia CIRP (2020).
[58] B. Jia, A. Rusinek, R. Pesci, S. Bahi, R. Bernier, Thermo-viscoplastic behavior of 304 austenitic stainless steel at various strain rates and temperatures: Testing, modeling and validation, International Journal of Mechanical Sciences 170 (2020) 105356.
[59] B. Gurrutxaga-Lerma, D.S. Balint, D. Dini, A.P. Sutton, The mechanisms governing the activation of dislocation sources in aluminum at different strain rates, Journal of the Mechanics and Physics of Solids 84 (2015) 273-292.
[60] A.H. Clausen, T. Børvik, O.S. Hopperstad, A. Benallal, Flow and fracture characteristics of aluminium alloy AA5083–H116 as function of strain rate, temperature and triaxiality, Materials Science and Engineering: A 364(1) (2004) 260-272.
[61] N. Sotirov, G. Falkinger, F. Grabner, G. Schmid, R. Schneider, R.J. Grant, R. Kelsch, K. Radlmayr, M. Scheerer, C. Reichl, H. Sehrschön, M. Loipetsberger, Improved Formability of AA5182 Aluminium Alloy Sheet at Cryogenic Temperatures, Materials Today: Proceedings 2 (2015) S113-S118.
[62] G.A. Edwards, K. Stiller, G.L. Dunlop, M.J. Couper, The precipitation sequence in Al–Mg–Si alloys, Acta Materialia 46(11) (1998) 3893-3904.
[63] N.K. Langhelle, J. Amdahl, Experimental And Numerical Analysis of Aluminium Columns Subjected to Fire, The Eleventh International Offshore and Polar Engineering Conference, International Society of Offshore and Polar Engineers, Stavanger, Norway, 2001, p. 8.
[64] S. Liu, A. Kouadri-Henni, A. Gavrus, Numerical simulation and experimental investigation on the residual stresses in a laser beam welded dual phase DP600 steel plate: Thermo-mechanical material plasticity model, International Journal of Mechanical Sciences 122 (2017) 235-243.
[65] G.R. Johnson, W.H. Cook, Fracture characteristics of three metals subjected to various strains, strain rates, temperatures and pressures, Engineering Fracture Mechanics 21(1) (1985) 31-48.
[66] LSTC, LS-DYNA keyword user's manual, Livermore Software Technology Corporation, California (2018).
[67] D. Li, A. Chrysanthou, I. Patel, G. Williams, Self-piercing riveting-a review, Int J Adv Manuf Technol 92(5-8) (2017) 1777-1824.
[68] S.M. Manladan, F. Yusof, S. Ramesh, M. Fadzil, Z. Luo, S. Ao, A review on resistance spot welding of aluminum alloys, Int J Adv Manuf Technol 90(1) (2017) 605-634.
[69] S. Fukumoto, I. Lum, E. Biro, D. Boomer, Y. Zhou, Effects of electrode degradation on electrode life in resistance spot welding of aluminum alloy 5182, Welding Journal 82(11) (2003) 307-S.
[70] L. Han, M. Thornton, M. Shergold, A comparison of the mechanical behaviour of self-piercing riveted and resistance spot welded aluminium sheets for the automotive industry, Materials & Design 31(3) (2010) 1457-1467.
[71] Henrob, 2018. http://www.henrob.co.uk/. (Accessed 04/12/2018).
[72] C.G. Pickin, K. Young, I. Tuersley, Joining of lightweight sandwich sheets to aluminium using self-pierce riveting, Materials & Design 28(8) (2007) 2361-2365.
[73] M. Kimchi, D.H. Phillips, Resistance spot welding: fundamentals and applications for the automotive industry, Synthesis Lectures on Mechanical Engineering 1(2) (2017) i-115.
[74] H. Eisazadeh, M. Hamedi, A. Halvaee, New parametric study of nugget size in resistance spot welding process using finite element method, Materials & Design 31(1) (2010) 149-157.